minerals

MDPI

Article

Partial Least Squares-Discriminant Analysis of the Major and Trace Elements and their Evolutionary Characteristics from the Jinchuan Ni-Cu-(PGE) Sulfide Deposit, NW China

Yuhua Wang [1], Jianqing Lai [1,*], Yonghua Cao [1], Xiancheng Mao [1], Xianghua Liu [1], Lu Peng [1] and Qixing Ai [2]

[1] Key Laboratory of Metallogenic Prediction of Nonferrous Metals and Geological Environment Monitoring (Ministry of Education), School of Geosciences and Info-Physics, Central South University, Changsha 410083, China
[2] Nickel Cobalt Research and Design Institute, Jinchuan Group Co. Ltd., Jinchang 737104, China
* Correspondence: ljq@csu.edu.cn; Tel.: +86-138-7598-3805

Abstract: The world-renowned Jinchuan Cu-Ni-(PGE) sulfide deposit consists of four mainly independent intrusive units from west to east, namely Segments III, I, II-W, and II-E, and the main sulfide types are the disseminated, net-textured, massive, and Cu-rich ores. Due to the similar geochemical characteristics of each segment, there is no convenient method to distinguish them and explain their respective variations. Meanwhile, considering that the division of different types of ores is confusing and their formation is still controversial, direct classification using elemental discrimination maps can facilitate subsequent mining and research. In this paper, we report the new major and trace elements data from the Jinchuan deposit and collect the published data to construct a database of 10 major elements for 434 samples and 33 trace elements for 370 samples, respectively, and analyze the data based on multivariate statistical analysis for the first time. Robust estimation of compositional data (robCompositions) was applied to investigate censored geochemical data, and the input censored data were transformed using the centered log-ratios (clr) to overcome the closure effect on compositional data. Exploratory data analysis (EDA) was used to characterize the spatial distribution and internal structural features of the data. The transformed data were classified by partial least squares-discriminant analysis (PLS-DA) to identify different compositional features for each segment and ore type. The receiver operator characteristic (ROC) curve was used to verify the model results, which showed that the PLS-DA model we constructed was reliable. The main discriminant elements were obtained by PLS-DA of the major and trace elements, and based on these elements, we propose the plot of SiO_2 + Al_2O_3 vs. CaO + Na_2O + K_2O and Cs + Ce vs. Th + U to discriminate the different segments of the Jinchuan deposit, and the Al_2O_3 + CaO vs. $Fe_2O_3^T$ + Na_2O and Co + Cu vs. Rb + Th + U to discriminate the different ore types. In addition, we predict that there are still considerable metal reserves at the bottom of Segment I.

Keywords: Jinchuan; Ni-Cu-(PGE) sulfide deposit; major and trace elements; compositional data analysis; PLS-DA

Citation: Wang, Y.; Lai, J.; Cao, Y.; Mao, X.; Liu, X.; Peng, L.; Ai, Q. Partial Least Squares-Discriminant Analysis of the Major and Trace Elements and their Evolutionary Characteristics from the Jinchuan Ni-Cu-(PGE) Sulfide Deposit, NW China. *Minerals* **2022**, *12*, 1301. https://doi.org/10.3390/min12101301

Academic Editor: Andrei Y. Barkov

Received: 19 September 2022
Accepted: 13 October 2022
Published: 16 October 2022

1. Introduction

Assembling and organizing existing data and using the statistical analysis to separate geochemical backgrounds and extract valuable information from redundant geological information has broad application prospects in geology. Most of the commonly available geochemical data are suitable for robust statistical classification methods, such as conventional multivariate statistical techniques, principal component analysis (PCA), and partial least squares-discriminant analysis (PLS-DA), which can effectively provide a brief description of high-dimensional data and highlight correlations between the variables [1–4]. The PLS-DA is a supervised classification technique using labeled data compared to the traditional analysis, which achieves maximum separation between categories by rotating the PCA components to reinforce the separation between observation groups, which in

turn identifies different categories of separated variables [2,5–10]. Currently, the discriminatory models are constructed by such methods to study the chemical composition of minerals such as magnetite [4,11], scheelite [12], tourmaline [13], and chalcopyrite [8], and to discriminate deposits and ore types such as the uranium deposits [14], gold deposits [15], magmatic Ni-Cu sulfide deposits [16,17], sphalerite [18], and lead-zinc deposits [19], as well as the ore-prospecting prediction [20,21].

The Jinchuan Ni-Cu-(PGE) sulfide deposit, located in NW China is the third largest magmatic Ni-Cu-(PGE) sulfide deposit in the world in mining after Noril'sk in Russia and Sudbury in Canada [22–24], and its pre-mining resources contain about 620 million tons (Mt) of sulfide ore at an average grade of 1.1 wt.% Ni and 0.7 wt.% Cu (Jinchuan Group Lit. 2017 latest reserve verification report). Since its discovery in 1958, its diagenesis and metallogenic process have been of great interest to geologists [17,23–32], resulting in the accumulation of a large amount of geochemical data. However, few scholars have used relevant statistical methods to "mine" the geochemical data, considering that the mineral and geochemical composition of Jinchuan's segments are similar [24,28–30,33], and the ore bodies are also influenced by late hydrothermal and tectonic processes [26,28,34,35]. There are still many controversies about the key processes of Jinchuan deposit formation, such as magma contamination, sulfide segregation, and fractional crystallization of olivine, etc. [23,27,32,36–39], and it is difficult to distinguish the various segments by the geochemical methods. In addition, the delineation of different types of ores is confusing and the mechanism of formation of different ore types is still unclear [40–43], which is one of the indicators that determines the economic production of the mining company, the analysis of which is necessary.

In this study, we used the X-ray fluorescence (XRF) and the inductively coupled plasma mass spectrometry (ICP-MS) to measure the whole-rock major and trace element compositions of the four segments from the Jinchuan deposit, and combined with the existing data, a geochemical database was established. This database was studied by using the PLS-DA to identify the geochemical characteristics between each segment and different ore types, and to analyze its role on the mineralization process, so as to provide ideas for a deep-seated mineral search in the Jinchuan deposit.

2. Geological Background

2.1. Regional Geology

The main intrusion of the Jinchuan Ni-Cu-(PGE) sulfide deposit is located within the Longshoushan terrane, which is NW-SE oriented and belongs to the southwestern part of the North China Craton (Figure 1a). The relationship between its geological setting and the deposits has been extensively described by previous authors [26–31,36,37,44,45] and is only briefly described in this paper. The Longshushan terrane has been deposited with strata ranging from the Neoproterozoic to Paleozoic sedimentary rocks (e.g., conglomerates, sandstones, limestones) (Figure 1b) [26]. The basement construction units of the Longshoushan Terrane are divided into the Baijiazuizi and Tamazigou formations, of which the Baijiazuizi formation is the direct envelope of the Jinchuan mafic–ultramafic intrusions and contains a large amount of migmatites, marbles, and gneisses [26,29].

The basement tectonics of the Longshoushan Terrane are dominated by NWW-oriented folds and faults, consistent with regional tectonic lines. The development of strong plastic flattening and permeable flow cleavage reflects the orogenic movement [26,46]. There are magmatic activities in the deposit from the Paleogene to the Mesozoic, with the largest area of granite (Figure 1b). On both sides of the terrane, there are magnesian–ultramafic rocks of different sizes and scales, as well as diorite, gabbro, and diabase, mostly as walls or along veins. Jinchuan and Zangbutai in particular have the largest exposure area [25,26,29,44]. The metallogenic age of the Jinchuan deposit is Neoproterozoic [23,47–49], with an available zircon U-Pb age of 831.8 ± 0.6 Ma [49].

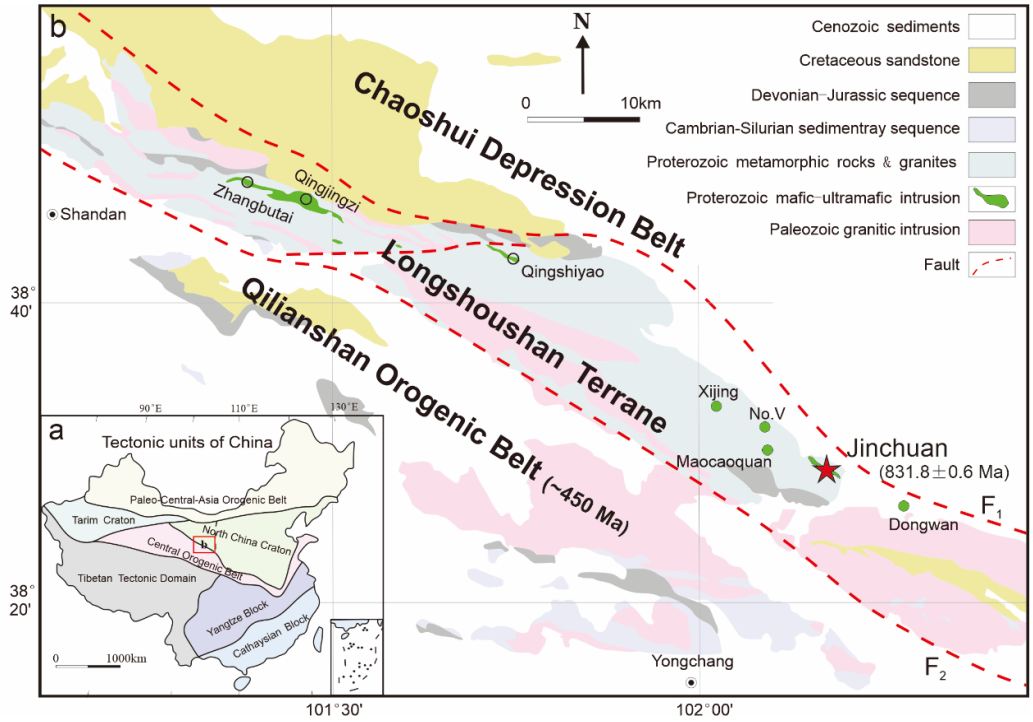

Figure 1. (**a**) The tectonic map showing the location of the Jinchuan Ni-Cu–(PGE) sulfide deposit in China and (**b**) the simplified regional geologic map of the Longshoushan terrane (modified from [31]). The zircon U-Pb ages of mafic-ultramafic intrusions are from [23,49–51].

2.2. Ore Deposit Geology

The F_1 fault in the NWW-oriented NE boundary of the Longshoushan reversible thrust structure formed by the Jinchuan deposit represents the main tectonic lineage direction of the segment (Figure 2a). The original production of the orebody is nearly horizontal [29,38], and the high angle SW tilt of the ore body is the result of the late uplift and overall subluxation of the rock body and stratigraphy [29,46,52]. As a series of NE-trending strike-slip faults—F_8, $F_{16\text{-}1}$, F_{23}—divide the Jinchuan deposit from west to east into the Segments III, I, II and IV (Figure 2b), the ore-bearing intrusions are roughly flared upwards in profile, wide at the top and narrow at the bottom (Figure 2c).

Segment III is located to the west of the F_8 fault and becomes shallow to acutely extinct to the west (Figure 2b). Based on the range of olivine grain size and the sharp contact surface between them, it can be divided into two cyclones: the upper and lower cycle [29]. The upper cycle is composed of fine-grained (0.5–3 mm) olivine and sulfide accumulation with minor pyroxene, and the lower cycle is composed of coarse-grained (6–10 mm) lherzolite intercalation and sulfide [24,29,30]. Disseminated and net-textured ores are distributed at the base of the segment, and the ore layers all thicken to the east, suggesting that the ore body may extend to Segment I [30], with rare massive ores (Figure 2c). Segment I extends from the F_8 fault in the west to the $F_{16\text{-}1}$ fault in the east, widening in the west and narrowing in the east (Figure 2b). The lithology can also be divided into two cycles, with the upper cycle consisting of fine-grained dunite and minor sulfides accumulating between olivine and pyroxene grains [24,29,31]. The lower cycle consists of coarse-grained lherzolite and abundant sulfide ores, with disseminated ores thin in the east and thickening to the west, extending into the III zone (Figure 2b). Below the disseminated ores are the net-textured ores several tens of meters thick, with the ore body thinning to the west [29]. The Cu-rich ores are distributed in the middle to lower part of the net-textured ores, which are produced in a lenticular shape and are clearly influenced by the tectonics [24,30,31].

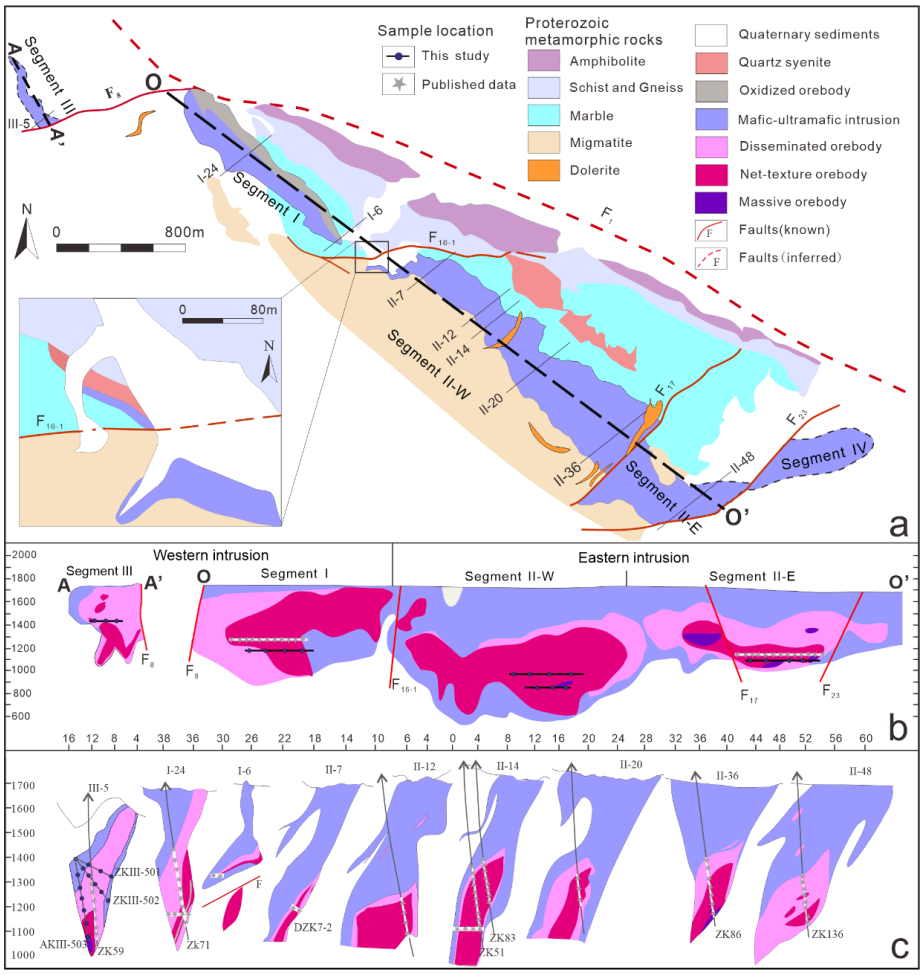

Figure 2. (**a**) Geological map of the Jinchuan deposit (Modified after [23]). (**b**) The projected long section and (**c**) selected the typical cross sections.

The east of the F_{16-1} fault is divided into Segments II and IV by the F_{23} fault (Figure 2b) and is much wider than the segment to the west. Segment II-W is divided into Segments II-W and II-E by the ore-free zone at row 28 of Segment II. The occurrence of Segment II-W is steep, with an angle of more than 40°. It consists of an upper and lower cycle, and the extension depth of the upper cycle is large (300–400 m) (Figure 2b,c) [26,29,31], which is mainly the weakly disseminated ores, wrapped by the coarse-grained lherzolite, and the coarse-grained pyroxene is also found near the edge of the Segment II-E [29,31]. The lower cycle is approximately 4 times larger than the upper cycle and extends to a depth of 200 m to >1100 m [26], in which there is a huge scale of net-textured ores, while massive ores are rare. Segment II-E is shallow (600–850 m) and the cross-section is similar to that of Segment II-W (Figure 2b), and the lithology is mainly dunite and lherzolite, with a clear boundary between them [29–31]. The sulfide accumulation is at the bottom and is distributed in concentric shells, similar to the II-W orebody [26], with the net-textured ores in the middle, surrounded by disseminated ores, and rare massive ores. Segment IV is located east of the F_{23} fault and has not been mined, so it is not included in this study.

3. Sampling and Description

The samples were collected from the newest mined locations in each segment in the Jinchuan deposit, and a total of 26 underground samples were collected along and/or through the vein in both directions. The collection locations were mainly: five samples from 1474 level near F_8 fault in Segment III; six samples from 1210 level in Segment I; four samples from middle section 934 level and four samples from 1018 level in Segment

II-W; and seven samples from 1110 level in Segment II-E east of F_{17} fault. In addition, the previous data were extensively collected for the study of geochemical characteristics and for the statistical analysis of the Jinchuan deposit.

Based on the variation of olivine content and the presence or absence of plagioclase content, the mafic–ultramafic intrusions (S < 0.3 wt.%) of the Jinchuan deposit (Figure 3a) are mainly classified as dunite, lherzolite, and minor olivine pyroxenite, etc. [26,29,31]. Dunite contains > 90% olivine, followed by pyroxene (1–8%) and a small amount of plagioclase (<2%). Lherzolite is the most dominant and the main rock type for sulfide mineralization in the Jinchuan deposit, consisting of about 40–85% olivine and 10–50% pyroxene (orthopyroxene > clinopyroxene), and olivine is usually medium to coarse grained (5–10 mm). The discovery of water-bearing minerals and quartz veins in the country rock is direct evidence of water-rich and volatile components in the upper part of the magma [26,28,34,35,52], suggesting that the Jinchuan were subjected to extensive hydrothermal alteration (Figure 3a). Sulfide-bearing ore types are based on the whole-rock S contents [30,31], and are mainly classified as the disseminated (0.3 < S < 5 wt.%) (Figure 3b), net-textured (5 < S < 25 wt.%) (Figure 3c), massive (S > 25 wt.%, chalcopyrite < 30 modal%), and Cu-rich ores (chalcopyrite > 50 modal%). Moreover, a small number of sulfides in isolated irregular or elongated bands filling the interstices of silicate minerals can also be found in the mafic–ultramafic intrusions (Figure 3d).

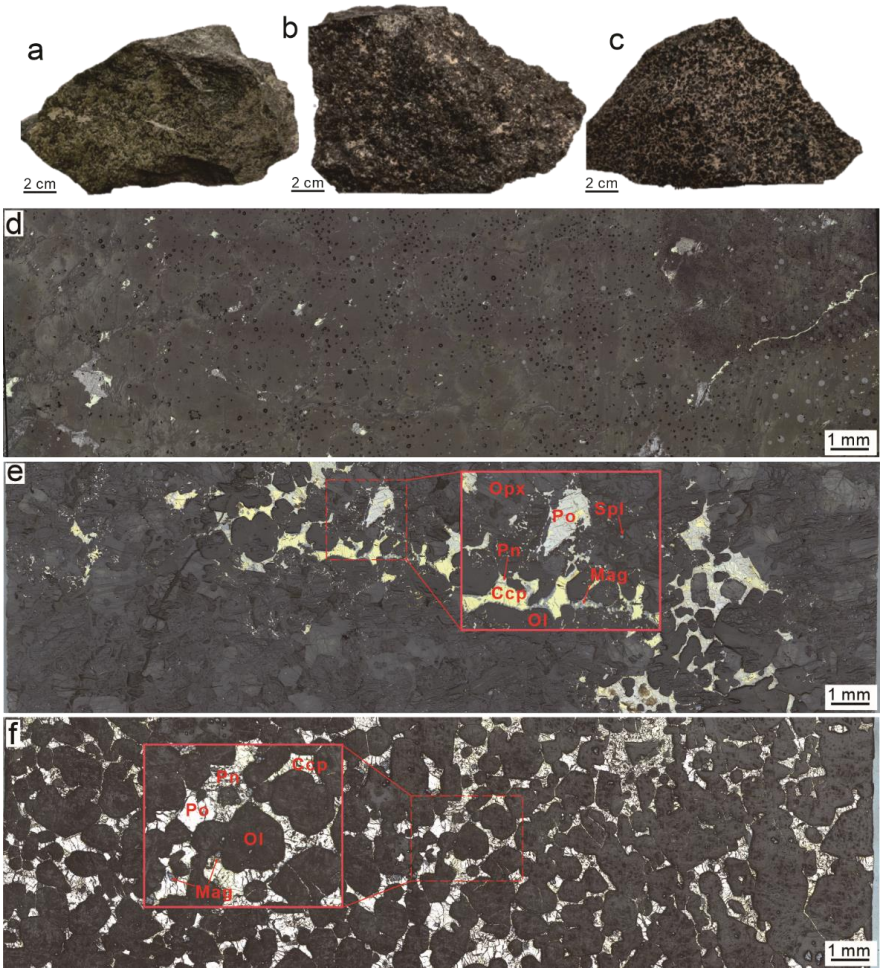

Figure 3. Photos of hand samples of the (**a**) mafic-ultramafic intrusions, (**b**)disseminated and (**c**) net-textured ores from the Jinchuan deposit. Scanned slab of the typical (**d**) mafic–ultramafic intrusion, (**e**) disseminated and (**f**) net-textured ores from the Jinchuan deposit. Ccp: chalcopyrite, Ol: olivine, Opx: orthopyroxene, Pn: pentlandite, Po: pyrrhotite, Spl: spinel, Mag: magnetite.

In the disseminated ore of the Jinchuan deposit, sulfides occur as irregularly shaped ellipsoidal droplets between silicate minerals and in interstitial patches, or as micro inclusions in silicate minerals (Figure 3e). Pyrrhotite is mainly filled in the sulfides, or a small amount is distributed in irregular shapes at the edges of the sulfides with cleavage decomposition, mainly hexagonal pyrrhotite. Chalcopyrite, on the other hand, is usually developed on the edges of pentlandite crystals or within inclusions (Figure 3e). Pentlandite occurs as distinctive grains or exsolved sheet crystals with a developed decomposition, mainly at the edges of chalcopyrite or pyrrhotite. Magnetite is mainly filled in patches within pentlandite or in microfractures in marginal sulfide (Figure 3e). Sulfide minerals in net-textured ores are developed in the interstices of olivine, pyroxene, and plagioclase, sometimes with the sulfides encasing isolated olivine (Figure 3f). Pyrrhotite in an irregular shape on the edge of sulfide is developed with cracks, while magnetite in the middle of the sulfides has a relatively smooth surface (Figure 3f). Chalcopyrite occurs at the edges of pyrrhotite crystals or in contact with silicates. Pentlandite usually occurs as fine grains clustered together and is distributed at the edges of chalcopyrite or pyrrhotite. Magnetite is irregularly elongated at the margins of sulfides, while it is mainly tetrahedral in the sulfides (Figure 3f). Massive ores and Cu-rich ores are not distributed much in the Jinchuan deposit, which is overall agglomerated and identified by relatively high amounts of chalcopyrite, magnetite pyrite, and pentlandite [30,36]. Because of the smaller samples of massive and Cu-rich ores, they were not statistically analyzed.

4. Analytical Methods

The samples were tested for major and trace elements at the ALS Chemex Co Ltd., Guangzhou, China. First, the sample was pulverized to less than 200 mesh in the pulverizer equipped with a ceramic plate or a disc mill using an alumina or agate chamber. The major elements were analyzed by X-ray fluorescence (XRF) with the test instrument PANalytical Axios Max, PANalytical B.V., Almelo, Netherlands, with an X-ray tube operating voltage of 40 kV and an operating current of 70 mA. The sample was dried at 105 °C, weighed accurately, placed in a platinum crucible, lithium tetraborate–lithium metaborate–lithium nitrate mixed melt was added, and that the sample and the melt were well mixed was confirmed. The sample was melted at 1050 °C in a high precision melting machine, the melt was poured into a platinum mold, cooled to form a melt sheet, that the quality of the melt sheet was qualified was confirmed, and then the concentration of major elements by the XRF was confirmed. To ensure the accuracy of the test, the ALS used a larger size of platinum mould. At the same time, another dried specimen was accurately weighed, aerobically cauterized at 1000 °C in a muffle furnace, and then accurately weighed after cooling, and the weight difference between the specimen before and after cauterization was the loss-on-ignition (LOI). Reference standards GBW07105 and SARM-4 were used to monitor the analysis of the major elements. Standard deviation was better than 5% and precision was better than 5%.

The trace elements were measured by inductively coupled plasma mass spectrometry (ICP-MS) with an instrument of Agilent 5110, Agilent Technologies Inc., Santa Clara, CA, USA. In order to ensure the accuracy of the test, the sample was divided into two parts, one part was decomposed with perchloric acid, nitric acid, and hydrofluoric acid, and the sample was evaporated to near dryness and dissolved in dilute hydrochloric acid to fix the volume, and then analyzed by Plasma emission spectroscopy and ICP-MS. The other part was added to the lithium metaborate/lithium tetraborate melt, mixed well, and melted in a furnace at 1025 °C or higher. After the melt was cooled, it was fixed with nitric acid, hydrochloric acid, and hydrofluoric acid, and then analyzed by ICP-MS. Depending on the actual condition of the sample and the effect of the digestion, the combined value was the final result of the assay. The standard OREAS-120 and OREAS-100a were used as reference standards to monitor the trace element analysis. The accuracy and precision for most of the measured elements were better than 3% and 5%, respectively. The concentrations of major and trace elements in different segments of the Jinchuan deposit are listed in Table S1.

5. Statistical Analysis

5.1. Pre-Processing of Compositional Data

Raw geochemical data may contain values below the detection limit (DL) and therefore they need to be filtered and adjusted before statistical analysis and interpretation [53]. Different methods have been proposed to interpolate the censored data, such as the exclusion of censored data or arbitrary substitution which are commonly used; however, they introduce statistical bias after aggregated estimation [53,54]. In this study, the method of Makvandi et al. (2016) [4], using the robCompositions R-package, was used to transform the results of the whole-rock major and trace elements data, including up to 40% of the censored data. In this approach, the k-nearest neighbors (impKNNa) function is used to estimate deletion values using the Aitchison distance [54–56]. The median value of the corresponding data based on unchecked neighbors with $k \geq 1$ is interpolated, and the error between the calculated random estimate and the original value determines the k value, with the optimal k yielding the smallest error, and the estimate usually greater than the lower DL, but never more than 3 times the DL, and always in the low precision range.

In addition, the geochemical data are typically compositional data with the "closure effect", i.e., the total of all components (elements) is equal to 1 (100%), and the components are constrained to each other, showing negative or positive spurious correlations [1,57]. The most popular method is to perform a logarithmic transformation to open the component data. The centered-log ratios (clr) used in this study were symmetric transformations with an orthogonal basis [4,58,59], which is applicable to the multivariate statistical techniques such as PCA, PLS-DA, etc. Finally, after the data pre-processing, the 434 samples of major elements and the 370 samples of trace elements were obtained.

5.2. Partial Least Squares-Discriminant Analysis (PLS-DA)

The partial least squares-discriminant analysis (PLS-DA) consists of classical PLS regression, which models the response matrix (Y) through the predictive matrix (X) [6]. PLS-DA is an alternative method when traditional multiple linear regression (MLR) is not applicable due to the highly correlated structure of the data. The Y matrix in PLS-DA is a set of binary variables (0 and 1) describing the observed categories [4,6], and the discriminant analysis determines which variables distinguish between two or more naturally occurring categories. PLS-DA allows for differentiation based on the properties of different observations and is a standard tool in chemometrics due to its ability to handle multicollinearity [3,6,60].

In the PLS-DA method, the objective is to extract a set of orthogonal components, the so-called latent variables, to correlate the X ($N \times K$) and Y ($N \times M$) matrices by maximizing the covariance between them using the following bilinear decomposition [6]:

$$X = TP' + E \quad (1)$$

$$Y = TD' + F \quad (2)$$

$$T = XW^* \quad (3)$$

where T ($N \times r$) contains r orthogonal PLS components and represents the common latent variable space of X and Y, P ($N \times r$), and D ($M \times r$) are the loading matrices of X and Y, respectively. W* is the so-called weight matrix and E and F are the model residuals of the X and Y matrices, respectively. These consist of the coefficients of linear combinations of the X variables, which are the most predictive of Y, i.e., linear combinations of elemental compositions that are the most discriminative of the deposit samples.

The variable contributions are the metrics that can be used to diagnose the cause of shifts from one cluster to another in the potential variable space or from the origin of a fractional scatter plot [61]. In this study, the contribution of constituent variables was calculated using Equation (4) to characterize the average composition of each sample group

and to identify differences in the average distribution of major or trace elements across minerals between samples in the potential variable space [6]:

$$C_k = (X_a - X_b)\sqrt{\sum_i \left(\frac{t_a - t_b}{s_{ti}}\right)^2 W_{ki}^2} \quad (4)$$

where C_k is the score contributions of variable k, X and t are the original variables and score values of sample (a), here the origin of the score plot and sample (b), respectively, W is the weighted value of variable k, and s corresponds to the standard deviation of the score vector i. The average composition of the sample set can be distinguished by the positive/negative contribution of the chemical elements, indicating higher/lower concentrations of the elements relative to the mean of the data set.

The parameter that summarizes the importance of each X variable on the category distinction is the variable importance on projection (VIP) [5] defined as:

$$VIP_k = \sqrt{\frac{K\sum_{a=1}^{r}\left(\left(\frac{W_{ak}}{\|W_a\|}\right)^2 (q_a^2 t_a' t_a)\right)}{\sum_{a=1}^{r}(q_a^2 t_a' t_a)}} \quad (5)$$

where K is the total number of X variables, W_{ak} is the weight of the k-th variable in the a-th principal component, r is the number of principal components. W_a, t_a, and q_a are the a-th column vectors of W and T and Q, respectively. VIP is the weighted sum of squares of PLS weights, which takes into account the amount of Y variance explained in each dimension. Variables with a VIP greater than 1 are the most influential in the model (classification), since the mean of squared VIP equals 1, and variables with VIPs between 0.8 and 1.0 represent moderately influential variables [3], while VIP values < 0.8 are less important.

To evaluate the reliability of the PLS-DA model, we plotted the receiver operating characteristic (ROC) curve, which has the horizontal coordinate of the false positive rate (FPR), i.e., 1-specificity, and the vertical coordinate of the true positive rate (TPR), i.e., sensitivity [60,62]. Among them, the AUC (area under the ROC curve, typically 0.5–1) is used as a summarized indicator of the ROC curve [8,63,64], and the larger the AUC value, the better the corresponding model (algorithm) performs. The AUC can be calculated as [62]:

$$AUC = \frac{1}{pn}\sum_{i=1}^{p}\sum_{j=1}^{n}\theta\left(Q_i^+, Q_j^-\right) \quad (6)$$

where $Q_i{}^+$, i = 1, . . . , p, and $Q_i{}^-$, j = 1, . . . , n, represent the anomaly scores of p positive observations (with deposit occurrence) and n negative observations (without deposit occurrence), respectively. θ ($Q_i{}^+$, $Q_i{}^-$) is the indictor function:

$$\theta\left(Q_i^+, Q_j^-\right) = \begin{cases} 1, & Q_i^+ > Q_j^- \\ 0.5, & Q_i^+ = Q_j^- \\ 1, & Q_i^+ < Q_j^- \end{cases} \quad (7)$$

6. Results

6.1. Geochemical Characteristics

6.1.1. Major Elements

The analysis results for major elements from the Jinchuan deposit are shown in Table S1. Combining the published data with the current data, the SiO_2 content of all samples from the Jinchuan deposit ranged from 16.60% to 68.19%, with an average of 35.23%; the MgO content ranged from 1.64% to 42.52%, with an average of 27.08%; the Al_2O_3 content ranged from 0.37% to 16.34%, with an average 3.47%; the content of K_2O ranged from 0.01% to 6.10%; the content of Na_2O ranged from 0.01% to 5.23%; and some were below the detection

line. The above characteristics indicate that the samples belong edto mafic–ultramafic rocks, the content of K_2O_3, Na_2O, and Al_2O_3 was low, and the content of MgO was high. The *m/f* values ((MgO + NiO)/($Fe_2O_3^T$ + MnO), molar) and $Mg^{\#}$ (100MgO/(MgO + $Fe_2O_3^T$), molar) values were relatively larger in Segments III and I compared with Segments II-W and II-E (Table S1).

In order to analyze the interrelationships between the major elements of each segment of the Jinchuan deposit, we selected the mafic–ultramafic intrusions samples (S < 0.3%), and because all samples had a large LOI, the 100% normalized data after deducting the LOI were used for analysis in this study. As shown in Figure 4, it can be seen that MgO was negatively correlated with CaO, Al_2O_3, and SiO_2, implying that magnetite is not the main crystallizing mineral during the crystallization of sulfides [26,36]. However, it was positively correlated with $Fe_2O_3^T$; the samples all plotted above the trajectories of olivine and plagioclase, indicating that it was related to the crystallization of forsterite (Figure 4b). The samples of mafic–ultramafic intrusions in Jinchuan deposit were mainly controlled by olivine, pyroxene, and a small amount of hornblende and plagioclase.

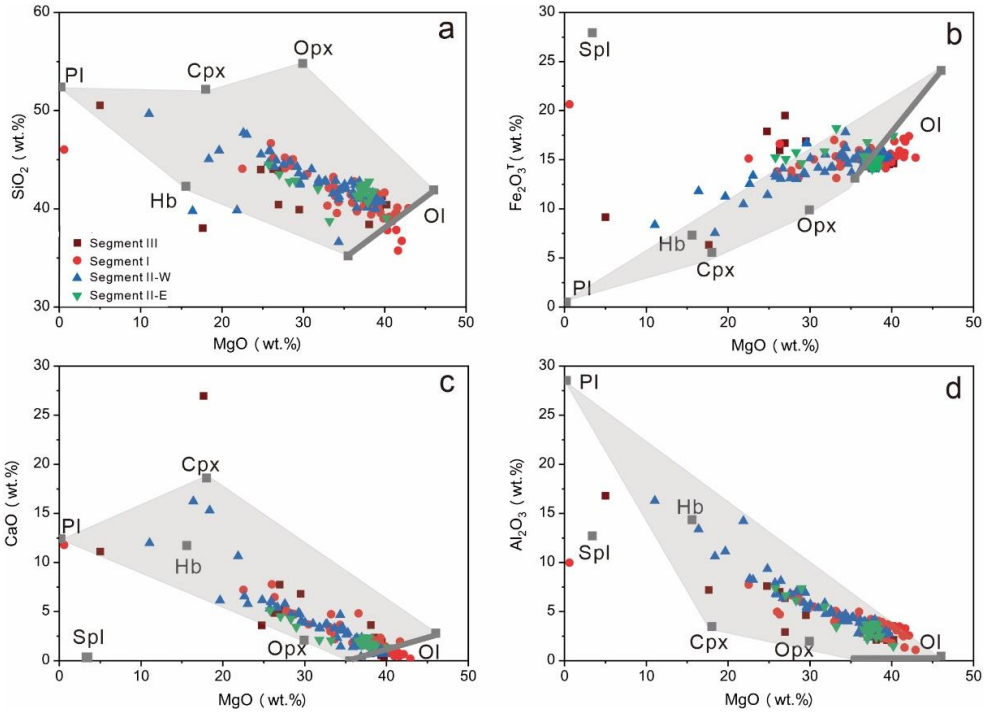

Figure 4. Harker diagram of the whole-rock major elements of mafic–ultramafic intrusions samples from the Jinchuan deposit. (**a**) MgO vs. SiO_2, (**b**) MgO vs. $Fe_2O_3^T$, (**c**) MgO vs. CaO, and (**d**) MgO vs. Al_2O_3. Data from this study and [23,29,36,38,44]. The chemical compositions of olivine (Ol), clinopyroxene (Cpx), orthopyroxene (Opx), spinel (Spl), plagioclase (Pl), and hornblende (Hb) are from [23,37,65–67].

6.1.2. Trace Elements

The trace elements contents of the samples tested are also listed in Table S1. The chondrite-normalized rare-earth elements (REE) and primitive mantle-normalized immobile trace element patterns of all samples from the Jinchuan deposit are illustrated in Figure 5. Trace elements were relatively enriched in large-ion lithophile elements (LILE) and low in high field strength elements (HFSE), and the negative anomalies of Nb and Sr were obvious, while the negative anomalies of Ba and positive anomalies of Th were mostly observed in Segments III and I, but the positive anomalies of Ba and no obvious anomalies of Th were observed in Segment II. The overall variation of rare-earth elements (REE)was relatively flat, and light rare-earth elements (LREE) were relatively enriched with slight positive or negative Eu anomalies; the trace element content of the mafic–ultramafic

intrusions samples was higher than that of sulfide-bearing samples in Segments II-W and II-E, while there was no significant difference between the trace element and REE contents of the samples in Segments III and I.

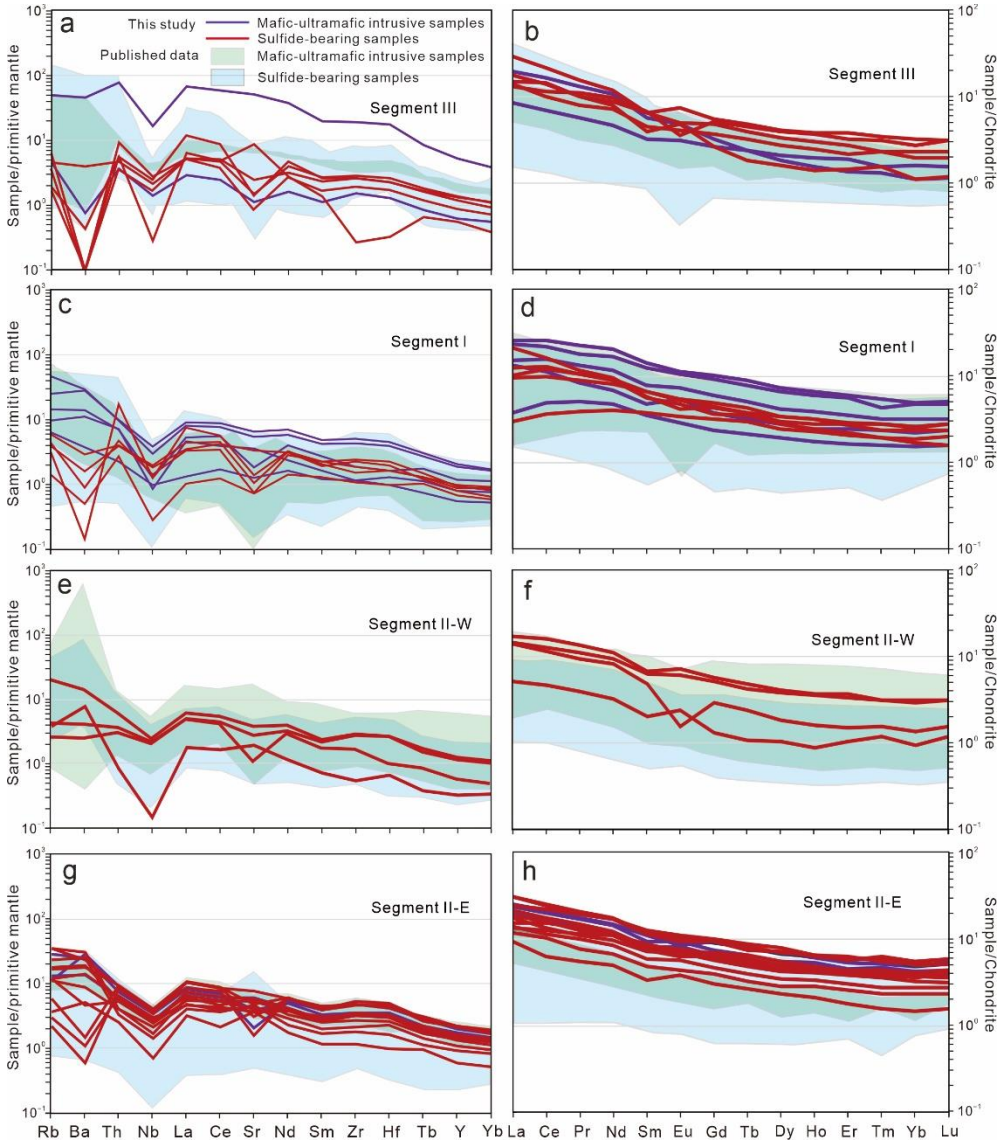

Figure 5. Primitive mantle-normalized trace element spider diagrams and chondrite-normalized rare-earth element (REE) patterns of the mafic-ultramafic intrusions and sulfide-bearing samples from (**a**,**b**) Segments III, (**c**,**d**) I, (**e**,**f**) II-W, and (**g**,**h**) II-E at the Jinchuan deposit. Data are from this study and [29,36,44,46,65]. The primitive mantle and chondrite standard values are from [68].

6.2. Exploratory Data Analysis

The geochemical data are often skewed when disturbed by "anomalies", which are partly caused by the uneven spatial distribution of crustal elements, secondly by the influence of various internal and external dynamic geological effects on element redistribution, and even by human activities [20,57]. In the statistical processing of the data, it is important to make the data obey normal or log-normal distribution as much as possible, and the variables have relative relationships with each other. The advantage of exploratory data analysis (EDA), which belongs to the category of robust statistics [20,69,70], is that it does not require the data to follow a normal distribution, and the internal structure of the data and the characteristics of the dispersion distribution can be quickly and accurately obtained by means of relevant graphical representations.

From the box plot diagrams (Figure 6), it can be seen that due to the large differences in the content of different elements in the original data, resulting in large variation in spatial scales, the data distribution was more scattered, and there were a large number of high-value outliers for elements with high content, while it was difficult to acquire useful information for elements with low content (Figure 6a,c). After the centered log-ratios (clr), the imbalance within the data was eliminated, making the data more concentrated and uniform (Figure 6b,d). In the cumulative density distribution curve (Figure 7), the cumulative density curve of the original data had a large difference in magnitude and scale between the data (Figure 7a,c). Similarly, the spatial distribution scale difference of each element was greatly reduced after clr transformation, which was in the same order of magnitude, and the spatial distribution was more uniform. The corresponding density curve was also approximately single- or multi-peaked with normal distribution (Figure 7b,d), which conforms to the requirements of multivariate statistical analysis. The average values of different ore types of major and trace elements for each segment in Jinchuan deposit obtained by pre-processing data (i.e., clr transformed data) are shown in Table 1.

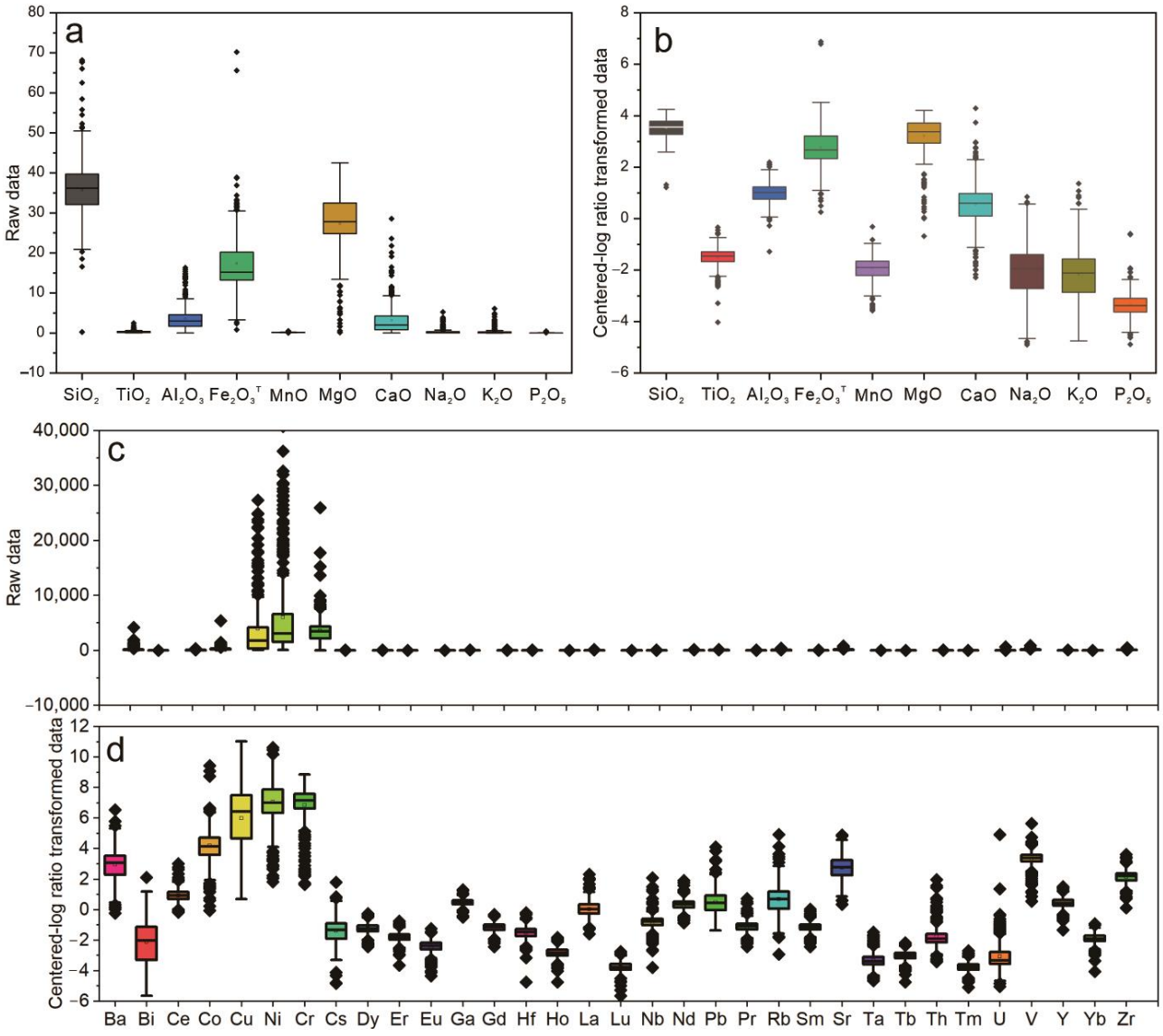

Figure 6. Box plot of raw (**a**,**c**) and centered-log ratios transformed (**b**,**d**) dataset. Data from this study, unpublished data and [17,23,24,29,31,36,38,44,46,65].

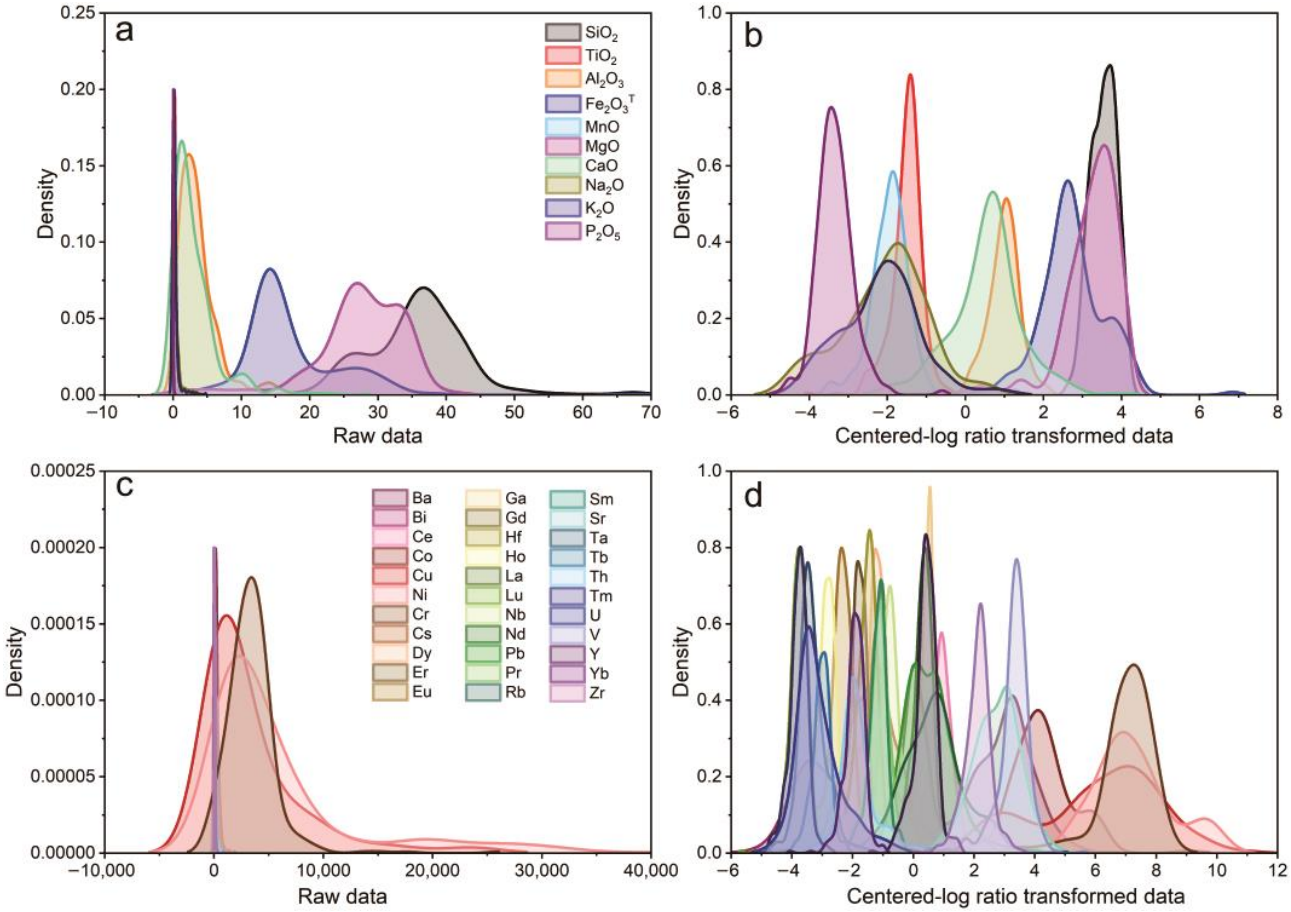

Figure 7. Density plot of raw (**a**,**c**) and centered-log ratios transformed (**b**,**d**) dataset. The data source is the same as Figure 6.

Table 1. Average values of major and trace elements for different ore types after data pre-processing from Jinchuan deposit.

Mining	Segment III			Segment I			Segment II-W			Segment II-E		
Type	**Ultr**	**Diss**	**Net**	**Ultr**	**Diss**	**Net**	**Ultr**	**Diss**	**Net**	**Ultr**	**Diss**	**Net**
n	**18**	**75**	**33**	**48**	**45**	**17**	**62**	**33**	**53**	**9**	**15**	**26**
SiO_2	43.52	36.76	28.26	39.25	37.26	28.59	40.18	35.75	29.78	37.89	37.54	27.98
TiO_2	0.59	0.27	0.15	0.32	0.26	0.14	0.40	0.31	0.16	0.26	0.29	0.18
Al_2O_3	7.73	3.43	1.61	3.93	4.10	1.27	5.53	4.30	1.56	2.86	3.69	1.86
$Fe_2O_3^T$	9.60	14.44	25.04	13.80	15.29	26.62	12.90	18.00	24.15	13.20	16.25	28.85
MnO	0.13	0.14	0.13	0.17	0.15	0.11	0.16	0.15	0.15	0.17	0.17	0.17
MgO	18.05	27.13	23.50	32.24	28.77	23.34	28.31	25.96	27.33	33.89	30.83	24.95
CaO	6.84	3.99	3.21	2.49	3.29	1.30	4.54	3.37	1.12	1.66	2.36	1.08
Na_2O	1.35	0.35	0.09	0.28	0.27	0.10	0.58	0.38	0.09	0.17	0.36	0.14
K_2O	1.27	0.34	0.09	0.34	0.24	0.05	0.44	0.30	0.08	0.13	0.19	0.10
P_2O_5	0.09	0.04	0.03	0.05	0.03	0.02	0.06	0.04	0.03	0.03	0.04	0.03
n	19	53	14	44	44	17	52	30	47	12	18	20
Ba	196.7	107.7	85.5	107.6	79.7	42.6	205.6	177.8	32.7	107.1	99.7	50.7
Bi	0.36	0.97	1.66	0.19	0.57	1.32	0.28	0.60	1.14	0.09	0.35	0.56
Ce	16.2	13.3	11.8	7.2	8.5	4.4	14.1	9.8	3.2	9.9	8.0	5.9
Co	167.5	196.4	333	126.7	319	444	142.9	253	388	147.0	191.7	432
Cu	1590	3358	6477	598	3354	17,103	1317	2778	7751	686	4556	4885
Ni	3550	4774	4942	1868	4940	16,555	2807	5966	13,553	1770	4187	12,341

Table 1. *Cont.*

Mining	Segment III			Segment I			Segment II-W			Segment II-E		
Type	**Ultr**	**Diss**	**Net**	**Ultr**	**Diss**	**Net**	**Ultr**	**Diss**	**Net**	**Ultr**	**Diss**	**Net**
n	**18**	**75**	**33**	**48**	**45**	**17**	**62**	**33**	**53**	**9**	**15**	**26**
Cr	2533	3330	1929	3194	4513	2840	4492	4692	3438	4238	3606	3153
Cs	0.91	0.98	0.53	2.20	1.07	0.34	2.21	1.59	0.47	1.32	1.06	0.36
Dy	1.37	1.09	0.82	0.90	1.11	0.47	1.66	1.21	0.39	1.05	0.88	0.63
Er	0.76	0.58	0.45	0.50	0.62	0.25	0.94	0.68	0.22	0.60	0.51	0.36
Eu	0.54	0.35	0.25	0.30	0.36	0.15	0.50	0.40	0.11	0.30	0.30	0.19
Ga	7.36	5.26	4.93	4.83	5.90	3.17	7.64	6.65	2.39	5.42	4.75	3.23
Gd	1.54	1.23	0.92	0.98	1.22	0.58	1.75	1.32	0.41	1.13	0.97	0.69
Hf	1.4	0.8	0.9	0.7	0.8	0.4	1.2	0.9	0.3	0.8	0.7	0.5
Ho	0.28	0.21	0.17	0.18	0.22	0.09	0.34	0.23	0.08	0.22	0.18	0.13
La	7.5	6.1	5.2	2.9	3.2	1.6	6.3	4.2	1.4	4.6	3.6	2.5
Lu	0.11	0.07	0.07	0.07	0.09	0.04	0.13	0.09	0.03	0.09	0.07	0.05
Nb	3.5	1.6	1.9	1.5	1.4	0.7	2.4	2.3	0.6	2.8	1.5	1.4
Nd	7.9	6.4	5.5	4.2	5.1	2.6	7.8	5.4	1.7	5.0	4.2	3.2
Pb	10.4	5.4	10.1	6.0	6.8	5.5	8.9	8.8	7.0	6.4	6.7	7.6
Pr	1.97	1.56	1.38	0.98	1.15	0.60	1.81	1.24	0.41	1.22	1.00	0.76
Rb	26.0	11.4	9.9	16.5	10.8	11.4	27.1	11.8	2.7	6.6	6.3	3.6
Sm	1.67	1.34	1.09	0.99	1.17	0.62	1.74	1.24	0.40	1.11	0.93	0.73
Sr	123.1	95.0	104.3	44.2	60.1	27.8	113.1	83.5	30.1	59.5	67.1	34.5
Ta	0.22	0.13	0.25	0.11	0.12	0.09	0.16	0.13	0.07	0.16	0.10	0.08
Tb	0.24	0.19	0.14	0.15	0.18	0.08	0.27	0.20	0.06	0.18	0.15	0.11
Th	1.29	1.28	2.55	0.68	0.80	4.13	0.99	0.55	0.20	0.47	0.39	0.32
Tm	0.11	0.08	0.07	0.07	0.09	0.04	0.13	0.10	0.03	0.09	0.07	0.05
U	0.47	0.41	0.50	0.39	0.18	0.33	0.31	0.13	0.06	0.11	0.10	0.08
V	111	84	62	82	114	57	134	110	48	65	72	67
Y	7.2	5.8	4.4	4.8	5.6	2.1	9.1	6.4	2.0	5.8	4.9	3.2
Yb	0.69	0.47	0.45	0.47	0.53	0.22	0.86	0.57	0.21	0.53	0.46	0.31
Zr	55	35	29	26	30	12	50	34	12	33	27	20

Notes: Unit of elemental content, all main elements are wt.%, all trace elements are ppm. Ultr: mafic–ultramafic intrusions, Diss: disseminated ore, Net: net-textured ore. n: number. Data sources as in Figure 6.

6.3. PLS-DA of Major and Trace Element Data of the Jinchuan Deposit

6.3.1. Characteristics of the Segment

Figure 8a shows the qw^*_1–qw^*_2 (first and second loadings) plots of the PLS-DA of the 10 major elements after the clr transformed data of the Jinchuan deposit. The results show that Segments III and I were positively correlated with Al_2O_3, CaO, and SiO_2, while TiO_2 and K_2O were weakly correlated, MgO and NaO_2 were positively correlated in the Segments II-W and II-E, MnO, $Fe_2O_3{}^T$, and P_2O_5 were weakly correlated. In the score plot (t_1–t_2), Segments III, I, and II-W were scattered in the plot, indicating that the major elements were variable depending on the different segment, while Segment II-W was clustered together and formed overlapping areas with other segments (Figure 8b). The first two latent variables explained about 60.4% of the variance of the 10 independent chemical variables (t_1 = 34%; t_2 = 26%, which together explained more than 50% of the variables considered reasonable). The score contributions plot (Figure 8c) shows that although the data overlapped in the score plot, the segments were still distinguishable due to the different average major compositions across the segments, e.g., SiO_2 had a high positive score contributions in Segment III, while it was negligible in Segment I, and vice versa in Al_2O_3. For the element selection, we followed the strategy proposed by Chong and Jun (2005) [5] and Wold and Eriksson (2005) [6], which combines VIP values (Figure 8d) and score contributions values (Figure 8c), indicating that variables are excluded only when both parameters are low. Therefore, SiO_2, Al_2O_3, CaO, NaO_2, and K_2O were selected as significant variables (K_2O was excluded due to low score contributions). The

ROC curves obtained from the cross-validation of the data (Figure 8e) confirmed the high reliability of the PLS-DA model to distinguish the segment.

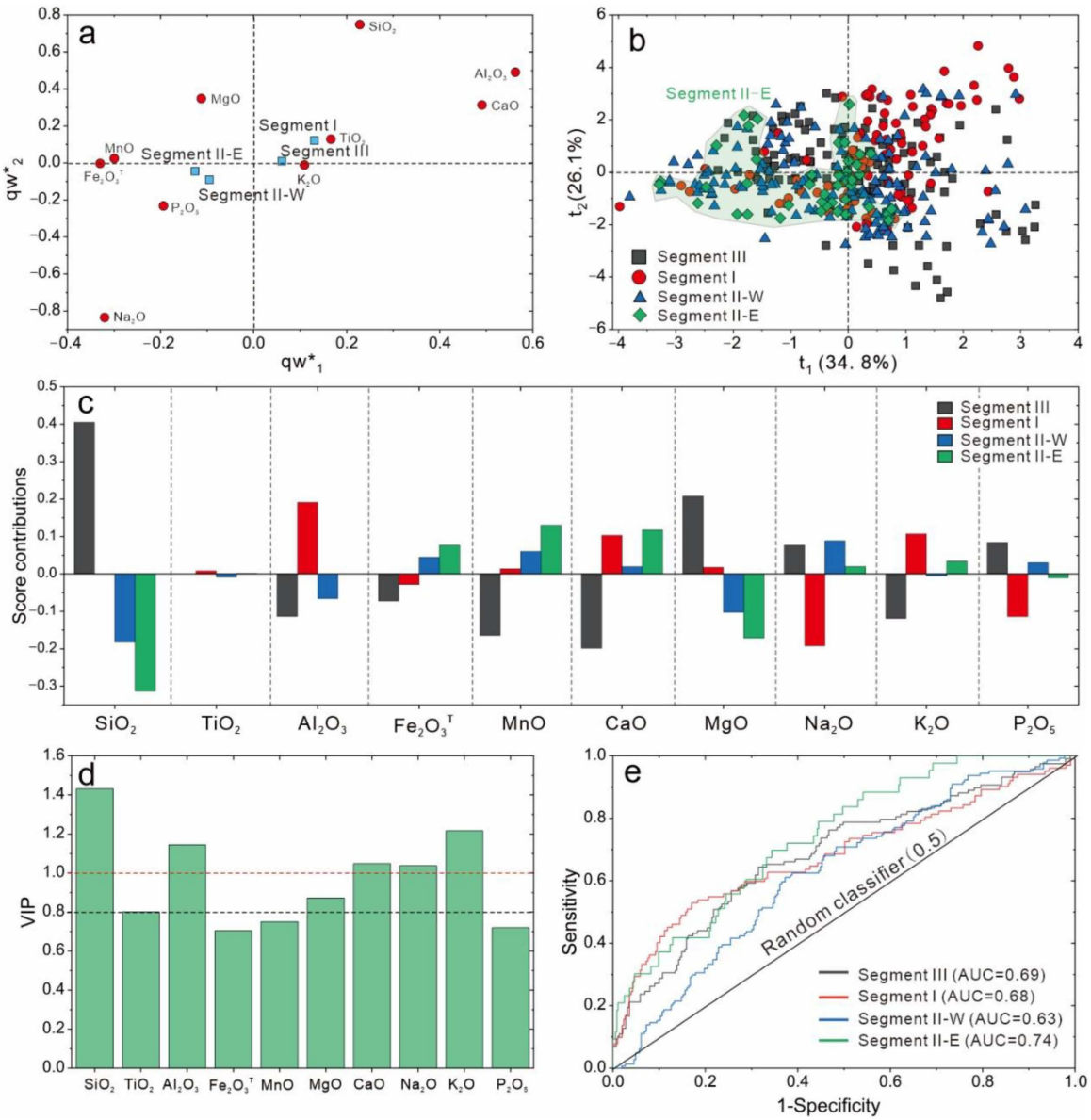

Figure 8. Partial least squares-discriminant analysis (PLS-DA) of whole-rock major element data in each segment from the Jinchuan deposit. (**a**) The qw^*_1–qw^*_2 (first and second loadings) plots show the correlation between elemental variables and the relationship between different elements and classification subgroups; loadings values indicate the influence of elements on classification, and the sign of the value indicates a positive or negative correlation between elements; and elements plotted at the far end of the loadings plot contribute most to the classification of subgroups in the score plot, while near the origin elements plotted near the origin have a negligible effect on the classification. (**b**) The t_1–t_2 (first and second scores) plot illustrate the sample distribution controlled by the correlation between samples in the loadings plot, with the green polygon circling the main areas of Segment II-E. (**c**) Score contributions plot, used to assess the association between predictor and response variables. (**d**) The variable importance on the projection (VIP) values reflects the significance of compositional variables for the classification of samples in the score plot (t_1–t_2), with the red dashed line in the VIP plot indicating a threshold of 1 and the black dashed line indicating a threshold of 0.8. (**e**) ROC curve for evaluating model effect. Data sources as in Figure 6.

Figure 9a shows the relationship between the 33 trace elements in qw^*_1 and qw^*_2 in the four segments of the Jinchuan deposit. It is clear that the Segment III showed more positively correlated elements than the other three segments, with strong correlations for Ba, Nd, Cs, Ce, La, Pr, and Sm, and strong positive correlations of Segments I, II-W, and II-E for Co,Ni, Cu, Bi, and Cr. In the score plot (Figure 9b), there was also considerable overlap among the four segments, where most of the samples from Segments III and I had higher t_2 values than Segments II-W and II-E, and were widely distributed. Similarly, Segment II-E showed also less variability. The elements Ba, Ce, Cr, Cs, La, Rb, Sr, Th, U, and V were interpreted as the significant variables, judged in combination with the score contributions values (Figure 9c) and VIP values (Figure 9d). The ROC curve (Figure 9e) confirmed the high reliability of the model in distinguishing the segments of the Jinchuan deposit, especially Segment III (AUC = 0.85).

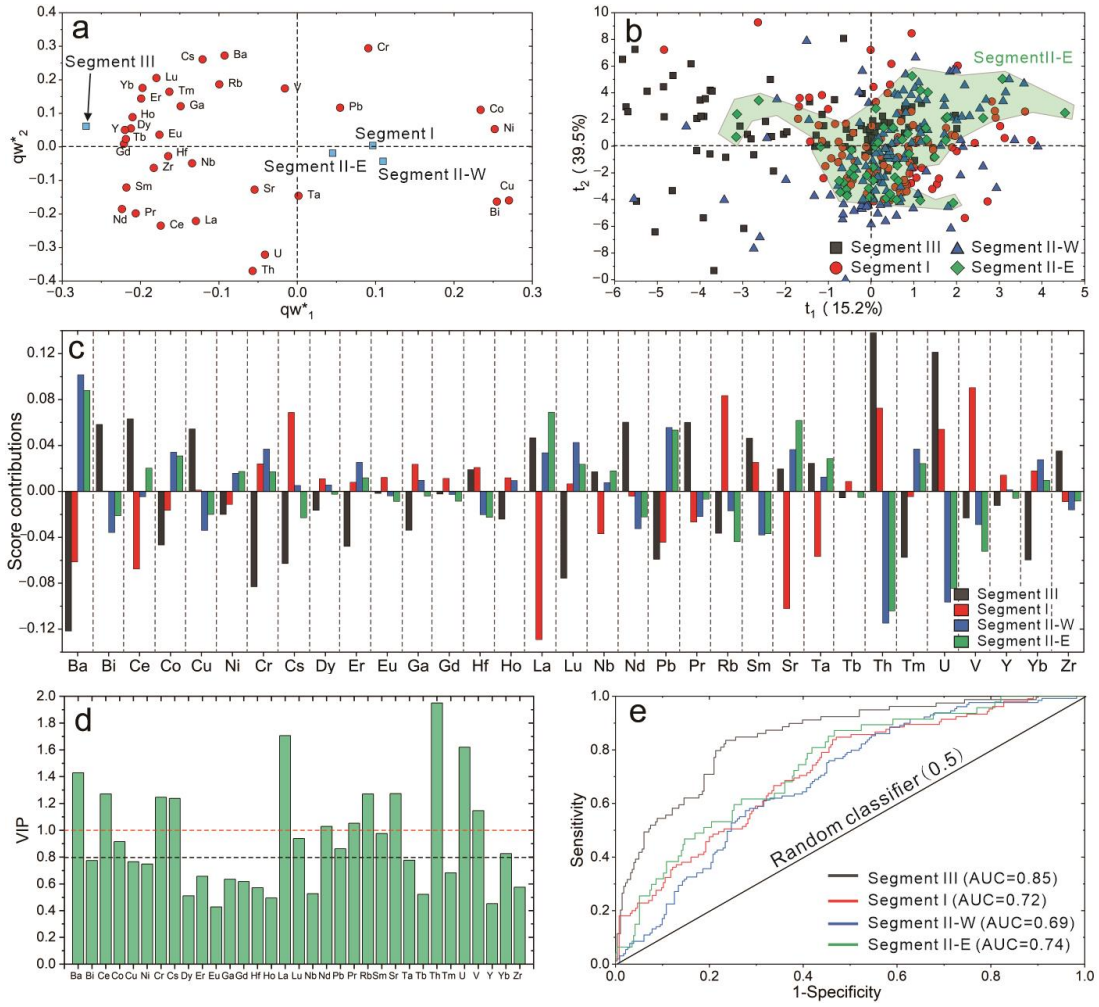

Figure 9. PLS-DA of whole-rock trace element data in each segment from the Jinchuan deposit. (**a**) The qw^*_1–qw^*_2 loadings plot; (**b**) The t_1–t_2 score plot; (**c**) The score contributions plot; (**d**) The VIP plot and (**e**) ROC curve.

6.3.2. Characteristics of Ore Type

In the major elements loading diagram by ore type (Figure 10a), the mafic-ultramafic intrusions and disseminated ores showed a strong positive correlation with Al_2O_3 and Na_2O, and net-textured ores had a positive correlation with MgO and $Fe_2O_3{}^T$. The first two scores explained 60.0% of the variables (Figure 10b), and three ore types could be distinguished depending on the t_1 values, with disseminated ores and mafic-ultramafic intrusions being widely distributed, and net-textured ores clustered mainly in areas with

negative t_1 and t_2 values. The highest content of Segment I was found in the score contributions of mafic–ultramafic intrusions (Figure 10c) and disseminated ores (Figure 10d). The disseminated ores had the lowest content of $Fe_2O_3^T$, TiO_2, K_2O, and P_2O_5 compared to the other two types in the score contributions (Figure 10d), while net-textured ores had a more uniform content in all segments. The combined score contributions plots (Figure 10c–e) and VIP plots (Figure 10f) distinguished Al_2O_3, $Fe_2O_3^T$, CaO, and NaO_2 as significant variables. In the ROC curves (Figure 10g), the models constructed by different ore types were reliable for each segment except for the disseminated ore in Segment III, which was poorly modeled (AUC = 0.56).

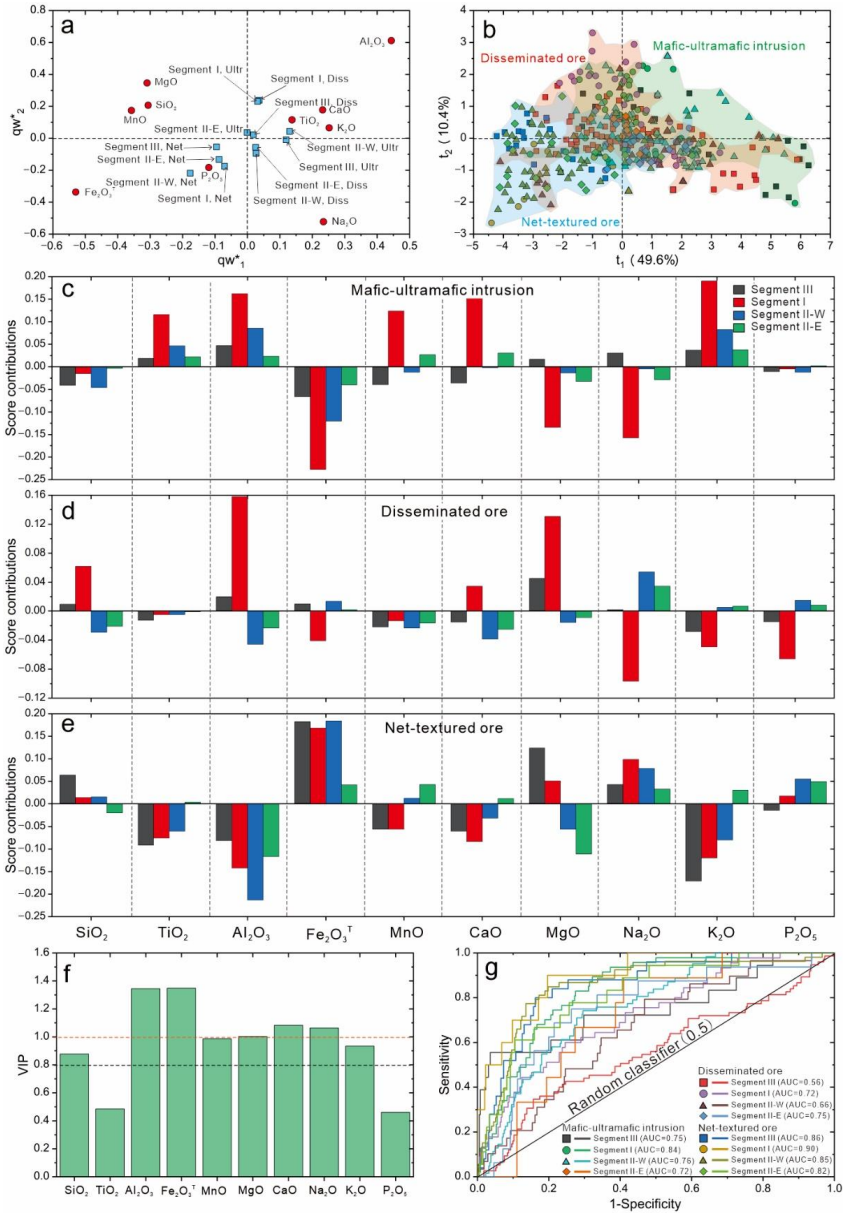

Figure 10. PLS-DA of whole-rock major element data for different ore types in each segment of the Jinchuan deposit. (**a**) The qw^*_1–qw^*_2 loading plots. (**b**) The t_1–t_2 score plots. The score contributions plots for (**c**) mafic–ultramafic intrusions, (**d**) disseminated ores, and (**e**) net-textured ores. (**f**) The VIP plots and (**g**) ROC curve. Ultr: mafic–ultramafic intrusions, Diss: disseminated ore, Net: net-textured ore.

In Figure 11a, it can be seen that the qw^*_1 values for the mafic–ultramafic intrusions were all negative, which had positive qw^*_2 values except for Segment III, and Th, U, Cu, Bi, and La were strongly correlated with the mafic–ultramafic intrusions; similarly,

the qw^*_1 and qw^*_2 values for the disseminated and net-textured ores were all positive, except for Segment III. Most of the samples had positive t_2 values, which allowed these three sulfide types to be distinguished sequentially by t_1 values (Figure 11b), and mafic–ultramafic intrusions had negative t_1 values, while the net-textured ores had positive t_1 values. Combined with the score contributions plots (Figure 11c–e) and VIP plots (Figure 11f), Ba, Bi, Ce, Co, Cu, Cs, Ni, La, Nd, Rb, Th, and U were interpreted as significant variables. The ROC curves (Figure 11g) could well separate the different ore types in each segment, confirming the reliability of the model.

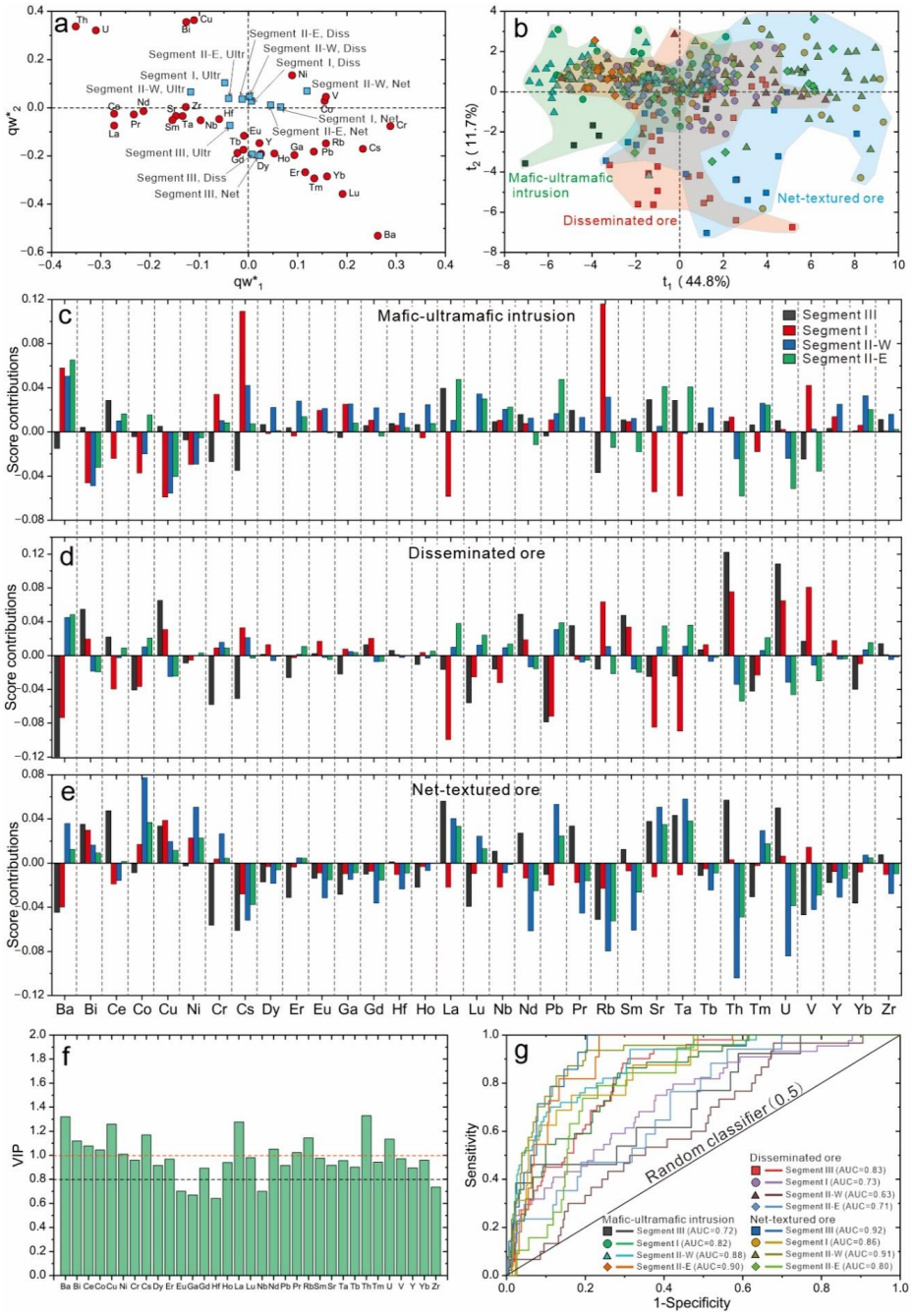

Figure 11. PLS-DA of whole-rock trace element data for different ore types in each segment of the Jinchuan deposit. (**a**) The qw^*_1–qw^*_2 loading plots; (**b**) The t_1–t_2 score plots. The score contributions plots for (**c**) mafic–ultramafic intrusions, (**d**) disseminated ores, and (**e**) net-textured ores. (**f**) The VIP plots and (**g**) ROC curve.

7. Discussion

7.1. Geochemical Variations among Segments of the Jinchuan Deposit

According to the PLS-DA model, it was found that most of the samples were clustered in the middle of the t_1–t_2 plot (Figure 8b), and the relatively low score contributions in MgO, $Fe_2O_3{}^T$, P_2O_5, K_2O, and TiO_2 (Figure 8c) were related to their similarity in the content in each segment. The VIP values and score contributions were calculated based on the whole model, including all original variables (elements) and latent variables; thus, the t_1–t_2 and qw^*_1–qw^*_2 plots only showed a small fraction of the variation in the entire data variables [4,8]. The inhomogeneous content of major elements in the samples of Segments III, I, and II-W led to the dispersion of the corresponding data points in the t_1–t_2 plots relative to Segment II-E (Figure 8b). This difference in content was the result of the non-homogeneity within each segment, reflecting the different thicknesses of their main intrusive horizons [24,29–31]. Al_2O_3, SiO_2, CaO, NaO_2, and K_2O could distinguish the four segments of the Jinchuan deposit (Figure 8c,d); the SiO_2 content could indicate that it is ultramafic, suggesting that its ultramafic degree increases from Segment III to Segment II-E, while Al_2O_3, Na_2O, and K_2O are usually used to judge the alkaline index of magmatic rocks, but the content of these elements in each segment was low, and it is difficult to distinguish them only by their contents (Table 1). Some the paragenetic minerals (such as pyroxene, hornblende, and apatite) are able to amplify these small changes and can be further analyzed for their rock-forming minerals or paragenetic minerals [26,37–39].

The Longshoushan terrane where the Jinchuan deposit is located was generated by mantle-derived magma in the continental rift zone of the southwest margin of the North China Craton [26,27] and confirmed to have originated in the open magma conduit system [23,24,27,29,31,46]. In recent years, the mineralogical, elemental, geochemical, and isotopic studies have shown that the parental magma in the Jinchuan deposit was the high-Mg picritic basaltic magma that originated from the partial melting of the enriched lithospheric mantle [26,30,47,52,65], which is generally enriched in LILE. This conclusion was confirmed by the relatively enriched LILE and low content of HFSE in the trace elements (Figure 5). According to the open magma system model, only 1% external material contamination is required to form the large sulfide bodies [40], with VIP values greater than 1 for Th, U, La, Sr, and Sm elements (Figure 9d) also indicating that the magma underwent a higher degree of crustal contamination during uplift, consistent with previous isotope-based studies [34,45,52]. It is noteworthy that the content of the Co, Cu, and Ni elements did not distinguish the differences between the segments (Figure 9d), even though the current production of these metals varies among the segments of the Jinchuan deposit.

7.2. Insights into Ore Types

The Al_2O_3, $Fe_2O_3{}^T$, K_2O, and Na_2O can distinguish the three ore types (Figure 10f), which are mainly present in pyroxene, olivine, and magnetite. Olivine is the most dominant cumulate mineral in the Jinchuan deposit, and the early fractional crystallization of olivine will go through a Mg-Fe exchange reaction with intergranular silicate melt, making its Fo decrease [37,71], With the fractional crystallization of olivine, it will settle with sulfide liquid due to gravity, and which undergoes gravity-driven seepage through the pore space of olivine cumulates and discharges the silicate melt upward, namely the disseminated ore. Some dense sulfide fluids may accumulate at the base of the crystalline paste, resulting in a net-textured structure (ore) or even the massive structure [41,42]. This process results in higher score contributions from the mafic–ultramafic intrusions to the net-textured ore $Fe_2O_3{}^T$ (Figure 10c–e). The lower score contributions of Al_2O_3 and K_2O are mainly reflected in the evolution of the paragenetic minerals, especially pyroxene, from the net-textured ore to the mafic–ultramafic intrusions, with higher Al_2O_3 content in pyroxene (Table 1), indicating the more evolved magma of the system [66].

Ba, Bi, Ce, Co, Cu, Ni, Cs, La, Nd, Pr, Rb, Th, and U are among the LILE that are chemically active and can easily migrate during mineralization, especially when fluid or volatiles are present. The Jinchuan deposit has been subjected to extensive hydrothermal alteration

and the presence of fluid volatiles has been identified [26,28,34,35,72]. The decompression during mineralization typically drives bubble nucleation (i.e., volatile degassing) [73,74], and the S-loss during degassing results in a reduction in sulfide fluid mass, which can significantly increase the silicate/sulfide mass ratio (i.e., R-factor) of the sulfide melt, thereby increasing the metal concentration in the sulfide phase [35,74,75]. In addition, the score contribution of these elements decreases from mafic–ultramafic intrusions to net-textured ores (Figure 11c–e), indicating that the mineralization environment of net-textured or massive ores is relatively closed and stable.

The Co, Cu, Ni, and Bi had elevated score contributions from mafic–ultramafic intrusions to net-textured ores from the Jinchuan deposit (Figure 10c–e), which indicates that their behavior is mainly influenced by the sulfide melts. The higher tenor of Cu, Ni, and PGE in disseminated ores compared to net-textured ores is due to the upgrading of these elements through the reaction between sulfide droplets and magma or due to a larger R-factor in the settling stage ratio [22,24,31,43,76]. The variation of Cu, Ni, and PGE grades in net-textured ores is due to the segregation and crystallization of sulfide liquids during percolation [24,43,77]. Meanwhile, the relatively high contribution of $Fe_2O_3{}^T$, Ni, and Co scores from the mafic–ultramafic intrusions (Figures 10c and 11c) may be due to the Fe-Ni (Co) exchange reaction that occurs between the segregation of the sulfide and olivine [23,37,71], resulting in increased Ni and Co contents in olivine.

7.3. Discrimination between Different Segments and Ore Types in the Jinchuan Deposit

Although the relationship between whole-rock major elements (Figure 4) and the trace element distribution diagram (Figure 5) can show the characteristics of a certain element and the relationship between elements more obviously, for example, further analysis of the minerals of the Jinchuan deposit can illustrate that they are the olivine-dominated cumulate rocks [37,39], there are more commonalities among the characterization in each segments, and it is difficult to account for the differences among them. Based on the PLS-DA of the whole-rock major and trace elements, we obtained several discriminating elements to distinguish different segments, namely SiO_2, Al_2O_3, CaO, Na_2O, K_2O, Ba, Ce, Cr, Cs, La, Rb, Sr, Th, U, and V (Figures 8 and 9). The elements indicating the degree of magmatic alkalinity (CaO, Na_2O, and K_2O), and the presence of crustal contamination (i.e., LILE) were selected by the above Section 7.1 analysis, and the SiO_2 + Al_2O_3 vs. CaO + Na_2O + K_2O and Cs + Ce vs. Th + U binary diagrams were proposed to distinguish the different segments of the Jinchuan deposit (Figure 12a,b). The results show that, in addition to the overlapping of Segments II-W and II-E, Segments III and I could be well distinguished from each other. This may be due to the ambiguity of the previous sampling locations of these two segments or the relatively smaller data of the Segment II-E. On the other hand, these two segments may themselves be the same intrusion [29,39].

We propose Al_2O_3 + CaO vs. $Fe_2O_3{}^T$ + Na_2O and Co + Cu vs. Rb + Th + U binary diagrams (Figure 12c,d) based on the discriminative elements selected by PLS-DA to distinguish the ore types of the Jinchuan deposit (Figures 10 and 11), considering the evolution trend among different ore types, the mineralization environment, and the content of elements (i.e., Co, Ni and Cu) as the discussion in Section 7.2. The results show that these ore types can be well distinguished except for a small number of disseminated ore ores. The new discriminant binary diagrams based on the PLS-DA results of this study, in addition to the PLS-DA model, can also be used as a complementary tool to characterize the differences between different segments and ore types in the deposit. As it should be, the reliability of the diagram still needs more data to be verified.

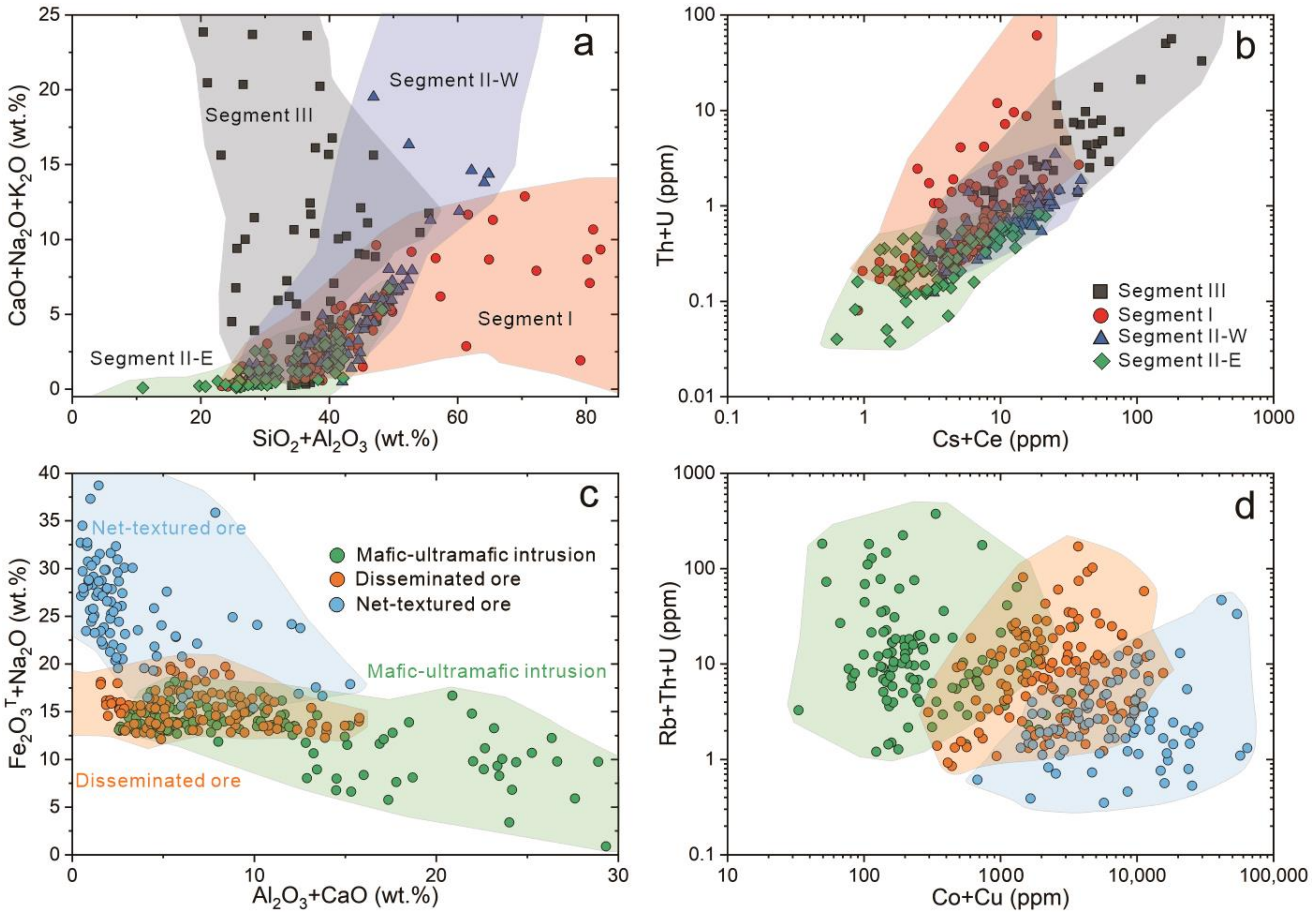

Figure 12. New discriminant binary diagrams, based on the PLS-DA results from this study, that could be used as complementary tools in prediction tasks in addition to PLS-DA models. Plot of the (**a**) SiO_2 + Al_2O_3 vs. CaO + Na_2O + K_2O and (**b**) Cs + Ce vs. Th + U to discriminate the different segment of Jinchuan deposit. Plot of the (**c**) Al_2O_3 + CaO vs. $Fe_2O_3{}^T$ + Na_2O and (**d**) Co + Cu vs. Rb + Th + U to discriminate the different ore types of Jinchuan deposit. Data sources as in Figure 6.

7.4. Implications for Deposit Exploration

Based on variations in the lithology and chemistry of the stratigraphy, Song et al. (2012) [29] divided the Jinchuan deposit into two separate intrusions with the $F_{16\text{-}1}$ fault as the boundary, and the later tectonic movement connects the two intrusions. Olivine growth is also different in these two intrusions, with various amounts of olivine crystals from Segment I transported from elsewhere and few or no olivine transported to Segments II-W and II-E [39].The similar distribution pattern (Figure 5) and the large overlap in the t_1-t_2 score plots (Figures 8b and 9b) of the four segments of Jinchuan deposit suggest the same parental magma, while the differences in most of the elemental correlations and score contributions indicate differences in the degree of magmatic evolution among the segments (Figures 8–11). This samples were low in HREE (Figure 5 and Table 1), which is presumed to have a deeper magmatic source area. Considering the location of the current sample collection (Figure 2b), Segments II-W and II-E were dominated by the collection of disseminated and net-textured ores, while Segments III and I were dominated by the collection of mafic–ultramafic intrusions and disseminated ores, which suggests that a large amount of sulfide melts may be retained at the bottom of the magma chamber. There is still potential to find ores in the deep or margins of the Jinchuan deposit [29,30]. It is important that Segment I and Segments II-W and II-E have similar characteristics in some trace elements (Figures 10 and 11), suggesting that a similar mineralization processes and

implying that there are also considerable metal reserves at its depth similar to the Segments II-W and II-E.

In summary, the multivariate statistical analysis can be used to investigate the data of elements commonly used in previous studies to identify important elements to provide assistance in deposit exploration. Although the location, age of formation, and source area characteristics of the ultramafic rocks associated with the Jinchuan deposit may be different, the multivariate statistical analysis or analogy with the Jinchuan deposit can be used to find out whether they have similar geochemical characteristics and to pick out the elements with a difference, which can provide ideas for the search for magmatic sulfide deposits.

8. Conclusions

In this paper, we constructed the PLS-DA model of the major and trace elements of the Jinchuan deposit to determine if there were differences among each segment and different sulfide ore types. Significant observations and conclusions of this work include the following:

(1) The preprocessed geochemical data had a more stable spatial distribution and internal structure than the raw data; the ROC values indicated the reliability of the established PLS-DA models for the major and trace elements;

(2) The main discriminant elements SiO_2, Al_2O_3, CaO, Na_2O, K_2O, Ba, Ce, Cr, Cs, La, Rb, Sr, Th, U, and V can distinguish the four segments of the Jinchuan deposit; the differences among the zones can be indicated by the alkalinity index, the degree of crustal contamination, and single minerals;

(3) The main discriminant elements Al_2O_3, $Fe_2O_3{}^T$, CaO, Na_2O, Ba, Bi, Ce, Co, Cu, Cs, La, Nd, Rb, Th, and U can distinguish the mafic–ultramafic intrusions, disseminated and net-textured ores, where Bi, Cu, La, Th, and U are strongly correlated with mafic–ultramafic intrusion, and Ba, Ni, and Cs are strongly correlated with disseminated and net-textured ores, indicating the evolution of the magma system from net-textured ores to mafic–ultramafic intrusions. The net-textured ores formed in a relatively closed and stable environment, where the fusion of sulfides and the segregation and crystallization of olivine controlled the enrichment of mineralizing elements;

(4) New discriminant binary diagrams, namely the plot of $SiO_2 + Al_2O_3$ vs. $CaO + Na_2O + K_2O$ and Cs + Ce vs. Th + U, can be used to discriminate the different segments of the Jinchuan deposit, and the plot of the Al_2O_3 + CaO vs. $Fe_2O_3{}^T + Na_2O$ and Co + Cu vs. Rb + Th + U can be used to discriminate the different ore types. In addition to the PLS-DA model, it can also be used as a complementary tool in prediction tasks;

(5) Segment I had some similar geochemical characteristics to Segments II-W and II-E of the Jinchuan deposit, suggesting that the enriched ore bodies may exist at depth.

Supplementary Materials: The following supporting information can be downloaded at: https://www.mdpi.com/article/10.3390/min12101301/s1, Table S1: The concentrations of major and trace elements of samples from the Jinchuan deposit.

Author Contributions: Conceptualization, Y.W.; data curation, Y.W.; formal analysis, Y.W.; funding acquisition, J.L. and Y.C.; investigation, Y.W.; methodology, Y.W.; software, Y.W.; writing—original draft, Y.W.; writing—review and editing, Y.W., J.L., Y.C., X.M., X.L., L.P. and Q.A. All authors have read and agreed to the published version of the manuscript.

Funding: This work was supported by grants from the National Natural Science Foundation of China (No. 41902077 and 42030809), the School-Enterprise Cooperation Scientific Research project of Jinchuan Group Co. Ltd. (No. JinKeDi 2020-07), and the Fundamental Research Funds for the Central Universities of Central South University (No. 506021723).

Data Availability Statement: Not applicable.

Acknowledgments: We thank Qiangzu Gao and Yulong Feng of the Nickel Cobalt Research and Design Institute, Jinchuan Group Co., Ltd. for sharing their knowledge about the local geology and their support during field work. Comments by the Editor and two anonymous reviewers helped improve the manuscript substantially, and they are gratefully acknowledged.

Conflicts of Interest: The authors declare no conflict of interest.

References

1. Aitchison, J. *The Statistical Analysis of Compositional Data*; Monographs on Statistics and Applied Probability; Chapman and Hall Ltd.: London, UK, 1986; 416p.
2. Mehmood, T.; Liland, K.H.; Snipen, L.; Sæbø, S. A review of variable selection methods in Partial Least Squares Regression. *Chemometr. Intell. Lab.* **2012**, *118*, 62–69. [CrossRef]
3. Eriksson, L.; Johansson, E.; Antti, H.; Holmes, E. *Multi- and Megavariate Data Analysis, Principles and Applications*; UMETRICS: Umeaa, Sweden,, 2001.
4. Makvandi, S.; Ghasemzadeh-Barvarz, M.; Beaudoin, G.; Grunsky, E.C.; McClenaghan, M.B.; Duchesne, C.; Boutroy, E. Partial least squares-discriminant analysis of trace element compositions of magnetite from various VMS deposit subtypes: Application to mineral exploration. *Ore Geol. Rev.* **2016**, *78*, 388–408. [CrossRef]
5. Chong, I.-G.; Jun, C.-H. Performance of some variable selection methods when multicollinearity is present. *Chemometr. Intell. Lab.* **2005**, *78*, 103–112.
6. Wold, S.; Sjöström, M.; Eriksson, L. PLS-regression: A basic tool of chemometrics. *Chemom. Intell. Lab. Syst.* **2001**, *58*, 109–130.
7. Ballabio, D.; Consonni, V. Classification tools in chemistry. Part 1: Linear models. PLS-DA. *Anal. Met.* **2013**, *5*, 3790–3798. [CrossRef]
8. Caraballo, E.; Dare, S.; Beaudoin, G. Variation of trace elements in chalcopyrite from worldwide Ni-Cu sulfide and Reef-type PGE deposits: Implications for mineral exploration. *Miner. Depos.* **2022**, *57*, 1293–1321. [CrossRef]
9. Barker, M.; Rayens, W. Partial least squares for discrimination. *J. Chemometr.* **2003**, *17*, 166–173. [CrossRef]
10. Brereton, R.G.; Lloyd, G.R. Partial least squares discriminant analysis: Taking the magic away. *J. Chemometr.* **2014**, *28*, 213–225. [CrossRef]
11. Huang, X.-W.; Sappin, A.-A.; Boutroy, É.; Beaudoin, G.; Makvandi, S. Trace element composition of igneous and hydrothermal magnetite from porphyry deposits: Relationship to deposit subtypes and magmatic affinity. *Econ. Geol.* **2019**, *114*, 917–952. [CrossRef]
12. Sciuba, M.; Beaudoin, G.; Grzela, D.; Makvandi, S. Trace element composition of scheelite in orogenic gold deposits. *Miner. Depos.* **2020**, *55*, 1149–1172.
13. Sciuba, M.; Beaudoin, G.; Makvandi, S. Chemical composition of tourmaline in orogenic gold deposits. *Miner. Depos.* **2021**, *56*, 537–560. [CrossRef]
14. Makvandi, S.; Huang, X.; Beaudoin, G.; Quirt, D.; Ledru, P.; Fayek, M. Trace element signatures in hematite and goethite associated with the Kiggavik-Andrew Lake structural trend U deposits (Nunavut, Canada). *Miner. Depos.* **2021**, *56*, 509–535. [CrossRef]
15. Liu, H.; Beaudoin, G. Geochemical signatures in native gold derived from Au-bearing ore deposits. *Ore Geol. Rev.* **2021**, *132*, 104066. [CrossRef]
16. Krivolutskaya, N.; Makvandi, S.; Gongalsky, B.; Kubrakova, I.; Svirskaya, N. Chemical characteristics of ore-bearing intrusions and the origin of PGE–Cu–Ni mineralization in the Norilsk Area. *Minerals* **2021**, *11*, 819. [CrossRef]
17. Mao, X.; Li, L.; Liu, Z.; Zeng, R.; Ai, Q. Multiple magma conduits model of the Jinchuan Ni-Cu-(PGE) deposit, northwestern China: Constraints from the geochemistry of platinum-group elements. *Minerals* **2019**, *9*, 187. [CrossRef]
18. Belissont, R.; Boiron, M.-C.; Luais, B.; Cathelineau, M. LA-ICP-MS analyses of minor and trace elements and bulk Ge isotopes in zoned Ge-rich sphalerites from the Noailhac—Saint-Salvy deposit (France): Insights into incorporation mechanisms and ore deposition processes. *Geochim. Cosmochim. Acta* **2014**, *126*, 518–540. [CrossRef]
19. Zhang, W.-D.; You, H.-T.; Li, B.; Zhao, K.-D.; Chen, X.-D.; Zhu, L. Ore-forming processes of the Qixiashan carbonate-hosted Pb-Zn deposit, South China: Constraints from sulfide trace elements and sulfur isotopes. *Ore Geol. Rev.* **2022**, *143*, 104786. [CrossRef]
20. Zheng, C.J.; Liu, P.F.; Luo, X.R.; Wen, M.L.; Huang, W.B.; Liu, G.; Wu, X.G.; Qiu, W.; Chen, Z.L.; Xiao, H.; et al. Rock geochemical data mining and weak geochemical anomalies identification—a case study of Ashele Copper-Zinc deposit, Xinjiang, NW China. *Geotect. Metall.* **2022**, *46*, 86–101, (In Chinese with English Abstract).
21. Liu, Y.; Zhu, L.; Ma, S.; Guo, F.; Gong, Q.; Tang, S.; Gopalakrishnan, G.; Zhou, Y. Constraining the distribution of elements and their controlling factors in the Zhaojikou Pb–Zn ore deposit, SE China, via fractal and compositional data analysis. *Appl. Geochem.* **2019**, *108*, 104379. [CrossRef]
22. Naldrett, A. *Magmatic Sulfide Deposits: Geology, Geochemistry and Exploration*; Springer: Berlin/Heidelberg, Germany; New York, HY, USA, 2004; pp. 1–744.
23. Duan, J. The Genesis and Metallogenic (PGE) Magmatic Model of JINCHUAN Cu-Ni Sulfide Deposit. Ph.D. Thesis, Chang'an University, Xi'an, China, 2015. (In Chinese).

24. Kang, J.; Song, X.-Y.; Long, T.-M.; Liang, Q.-L.; Barnes, S.J.; Chen, L.-M.; Li, D.-X.; Ai, Q.-X.; Gao, Y.-L. Lithologic and geochemical constraints on the genesis of a newly discovered orebody in the Jinchuan intrusion, NW China. *Econ. Geol.* 2022; in press.
25. Jia, E.H. Geological characteris tics of the Jinchuan Cu-Ni sulfide deposit in Gansu Province. *Miner. Depos.* **1986**, *5*, 26–38. (In Chinese with English Abstract).
26. Tang, Z.L.; Li, W.Y. *Metallogenic Model and Geological Comparison of Jinchuan Ni-Cu-(Pt) Deposit*; Geological Publishing House: Beijing, China, 1995; p. 208. (In Chinese)
27. Chai, G.; Naldrett, A. Characteristics of Ni-Cu-PGE mineralization and genesis of the Jinchuan Deposit, Northwest China. *Econ. Geol.* **1992**, *87*, 1475–1495. [CrossRef]
28. Su, S.; Li, C.; Zhou, M.-F.; Ripley Edward, M.; Qi, L. Controls on variations of platinum-group element concentrations in the sulfide ores of the Jinchuan Ni-Cu deposit, western China. *Miner. Depos.* **2008**, *43*, 609–622. [CrossRef]
29. Song, X.Y.; Danyushevsky, L.V.; Keays, R.R.; Chen, L.M.; Wang, Y.S.; Xiao, T.J.F. Structural, lithological, and geochemical constraints on the dynamic magma plumbing system of the Jinchuan Ni–Cu sulfide deposit, NW China. *Miner. Depos.* **2012**, *47*, 277–297. [CrossRef]
30. Chen, L.M.; Song, X.Y.; Keays, R.R.; Tian, Y.L.; Xiao, J.F. Segregation and fractionation of magmatic Ni-Cu-PGE sulfides in the western Jinchuan intrusion, northwestern China: Insights from platinum group element geochemistry. *Econ. Geol.* **2013**, *108*, 1793–1811. [CrossRef]
31. Song, X.-Y.; Keays, R.R.; Zhou, M.-F.; Qi, L.; Ihlenfeld, C.; Xiao, J.-F. Siderophile and chalcophile elemental constraints on the origin of the Jinchuan Ni-Cu-(PGE) sulfide deposit, NW China. *Geochim. Cosmochim. Acta* **2009**, *73*, 404–424. [CrossRef]
32. Han, Y.X. The Comparative Study on Platinum Group Elements in Jinchuan and Xiarihamu Magmatic Cu-Ni Sulfide Deposits. Ph.D. Thesis, Chang'an University, Xi'an, China, 2021. (In Chinese).
33. Li, C.; Ripley, E. The giant Jinchuan Ni-Cu-(PGE) deposit tectonic setting, magma evolution, ore genesis, and exploration implications. *Econ. Geol.* **2011**, *17*, 163–180.
34. Zhang, M.; Tang, Q.; Hu, P.; Ye, X.; Cong, Y. Noble gas isotopic constraints on the origin and evolution of the Jinchuan Ni–Cu–(PGE) sulfide ore-bearing ultramafic intrusion, Western China. *Chem. Geol.* **2013**, *339*, 301–312. [CrossRef]
35. Yang, S.-H.; Yang, G.; Qu, W.; Du, A.; Hanski, E.; Lahaye, Y.; Chen, J. Pt-Os isotopic constraints on the age of hydrothermal overprinting on the Jinchuan Ni-Cu-PGE deposit, China. *Miner. Depos.* **2018**, *53*, 757–774. [CrossRef]
36. Tonnelier, N. Geology and Genesis of the Jinchuan Ni-Cu-(PGE) Deposit, China. Ph.D. Thesis, Laurentian University, Sudbury, ON, Canada, 2010.
37. Li, C.; Xu, Z.; de Waal, S.A.; Ripley, E.M.; Maier, W.D. Compositional variations of olivine from the Jinchuan Ni–Cu sulfide deposit, western China: Implications for ore genesis. *Miner. Depos.* **2004**, *39*, 159–172. [CrossRef]
38. De Waal, S.; Xu, Z.G.; Li, C.; Mouri, H. Emplacement of viscous mushes in the Jinchuan ultramafic intrusion, western China. *Can. Mineral.* **2004**, *42*, 371–392. [CrossRef]
39. Mao, Y.; Barnes, S.; Duan, J.; Qin, K.-Z.; Godel, B.; Jiao, J. Morphology and particle size distribution of olivines and sulphides in the Jinchuan Ni–Cu sulphide deposit: Evidence for sulphide percolation in a crystal Mush. *J. Petrol.* **2018**, *59*, 1701–1730. [CrossRef]
40. Li, C.; Ripley, E.M.; Naldrett, A.J.; Schmitt, A.K.; Moore, C.H. Magmatic anhydrite-sulfide assemblages in the plumbing system of the Siberian Traps. *Geology* **2009**, *37*, 259–262. [CrossRef]
41. Barnes, S.J.; Cruden, A.R.; Arndt, N.; Saumur, B.M. The mineral system approach applied to magmatic Ni-Cu-PGE sulphide deposits. *Ore Geol. Rev.* **2016**, *76*, 296–316. [CrossRef]
42. Barnes, S.J.; Staude, S.; Le Vaillant, M.; Piña, R.; Lightfoot, P.C. Sulfide-silicate textures in magmatic Ni-Cu-PGE sulfide ore deposits: Massive, semi-massive and sulfide-matrix breccia ores. *Ore Geol. Rev.* **2018**, *101*, 629–651. [CrossRef]
43. Barnes, S.J.; Mungall, J.E.; Le Vaillant, M.; Godel, B.; Lesher, C.M.; Holwell, D.; Lightfoot, P.C.; Krivolutskaya, N.; Wei, B. Sulfide-silicate textures in magmatic Ni-Cu-PGE sulfi de ore deposits: Disseminated and net-textured ores. *Am. Mineral.* **2017**, *102*, 473–506. [CrossRef]
44. Song, X.-Y.; Zhou, M.-F.; Wang, C.Y.; Qi, L.; Zhang, C.-J. Role of Crustal Contamination in Formation of the Jinchuan Intrusion and Its World-Class Ni-Cu-(PGE) Sulfide Deposit, Northwest China. *Int. Geol. Rev.* **2006**, *48*, 1113–1132. [CrossRef]
45. Lehmann, J.; Arndt, N.; Windley, B.; Zhou, M.-F.; Wang, C.; Harris, C. Field relationships and geochemical constraints on the emplacement of the Jinchuan Intrusion and its Ni-Cu-PGE sulfide deposit, Gansu, China. *Econ. Geol.* **2007**, *102*, 75–94. [CrossRef]
46. Zeng, R.Y. Magma Conduit System and Magmatic Evolution of Jinchuan Cu-Ni Sulfide Deposit. Master's Thesis, Central South University, Changsha, China, 2014. (In Chinese).
47. Li, X.; Li, S.; Biao, S.; Dunyi, L. SHRIMP U-Pb zircon age of the Jinchuan ultramafic intrusion and its geological significance. *Chin. Sci. Bull.* **2004**, *49*, 420–422. [CrossRef]
48. Yang, G.; Du, A.; Lu, J.; Qu, W.; Chen, J. Re-Os (ICP-MS) dating of the massive sulfide ores from the Jinchuan Ni-Cu-PGE deposit. *Sci. China Earth Sci.* **2005**, *48*, 1672–1677. [CrossRef]
49. Zhang, M.; Kamo, S.L.; Li, C.; Hu, P.; Ripley, E.M. Precise U–Pb zircon–baddeleyite age of the Jinchuan sulfide ore-bearing ultramafic intrusion, western China. *Miner. Depos.* **2010**, *45*, 3–9. [CrossRef]
50. Jiao, J.G.; Jin, S.F.; Rui, H.C.; Zhang, G.P.; Ling, Q.F.; Shao, L.Q. Petrology, geochemistry and chronology study of the Xiaokouzi mafic-ultramafic in the eastern section of Longshou Mountains, Gansu. *Acta Geol. Sin.* **2017**, *91*, 736–747. (In Chinese with English Abstract).

51. Zeng, R.; Lai, J.; Mao, X.; Xiao, W.; Yan, J.; Zhang, C.; Hu, J.; Ai, Q. Petrogenesis and tectonic significance of the Early Devonian lamprophyres and diorites in the Alxa Block, NW China. *Geochemistry* **2020**, *81*, 125685. [CrossRef]
52. Jiao, J.G.; Liu, H.; Duan, J.; Lu, H.; Luo, Z.D.; Qi, D. Hf isotope geochemical characteristics and magma sources in Jinchuan Cu-Ni sulfide deposite. *J. Earth Sci. Environ.* **2014**, *36*, 58–67, (In Chinese with English Abstract).
53. Helsel, D. *Nondetects and Data Analysis: Statistics for Censored Environmental Data*; Wiley: New York, NY, USA, 2005; 268p.
54. Grunsky, E.; Drew, L.; Woodruff, L.; Friske, P.; Sutphin, D. Statistical variability of the geochemistry and mineralogy of soils in the Maritime Provinces of Canada and part of the Northeast United States. *Geochem-Explor. Environ. Anal.* **2013**, *13*, 249–266. [CrossRef]
55. Filzmoser, P.; Hron, K.; Reimann, C. Principal component analysis for compositional data with outliers. *Environmetrics* **2009**, *20*, 621–632. [CrossRef]
56. Bacon-Shone, J. A short history of compositional data analysis. In *Compositional Data Analysis: Theory and Applications*; Pawlowsky-Glahn, V., Buccianti, A., Eds.; John Wiley & Sons: New York, NY, USA, 2011; pp. 3–11.
57. Grunsky, E. The interpretation of geochemical survey data. *Geochem-Explor. Environ. Anal.* **2010**, *10*, 27–74. [CrossRef]
58. Egozcue, J.J.; Pawlowsky-Glahn, V.; Mateu-Figueras, G.; Barceló-Vidal, C. Isometric logratio transformations for compositional data analysis. *Math. Geol.* **2003**, *35*, 279–300. [CrossRef]
59. Pawlowsky-Glahn, V.; Egozcue, J.J. Compositional data analysis: How important are the sample space and its structure? In Proceedings of the Conference: Center for Microbiome Innovation June Seminar UCSD School of Medicine, La Jolla, CA, USA, 21–22 June 2018.
60. Westerhuis, J.A.; Hoefsloot, H.C.J.; Smit, S.; Vis, D.J.; Smilde, A.K.; van Velzen, E.J.J.; van Duijnhoven, J.P.M.; van Dorsten, F.A. Assessment of PLS-DA cross validation. *Metabolomics* **2008**, *4*, 81–89. [CrossRef]
61. Miller, P.; Swanson, R.; Heckler, C. Contribution Plots: A missing link in multivariate quality control. *Appl. Math. Comput. Sci.* **1998**, *8*, 775–792.
62. Bergmann, R.; Ludbrook, J.; Spooren, W. Different outcomes of the wilcoxon—mann—whitney test from different statistics packages. *Am. Stat.* **2000**, *54*, 72–77.
63. Nykänen, V.; Lahti, I.; Niiranen, T.; Korhonen, K. Receiver operating characteristics (ROC) as validation tool for prospectivity models—A magmatic Ni–Cu case study from the Central Lapland Greenstone Belt, Northern Finland. *Ore Geol. Rev.* **2015**, *71*, 853–860. [CrossRef]
64. Parsa, M.; Maghsoudi, A.; Yousefi, M. A receiver operating characteristics-based geochemical Data fusion technique for targeting undiscovered mineral deposits. *Nat. Resour. Res.* **2018**, *27*, 15–28. [CrossRef]
65. Chai, G.; Naldrett, A.J. The Jinchuan ultramafic intrusion: Cumulate of a high-Mg basaltic magma. *J. Petrol.* **1992**, *33*, 277–303. [CrossRef]
66. Chai, G.; Naldrett, A.J. Pyroxene mineral chemistry of the Jinchuan intrusion, China. *Miner. Petrol.* **1994**, *51*, 1–20. [CrossRef]
67. Kang, J.; Chen, L.M.; Yu, S.Y.; Zheng, W.Q.; Dai, Z.-H.; Zhou, S.-H.; Ai, Q.-X. Chromite geochemistry of the Jinchuan Ni-Cu sulfide-bearing ultramafic intrusion (NW China) and its petrogenetic implications. *Ore Geol. Rev.* **2022**, *141*, 104644. [CrossRef]
68. McDonough, W.F.; Sun, S.S. The composition of the earth. *Chem. Geol.* **1995**, *120*, 223–253. [CrossRef]
69. Shi, C.Y. Appication of the exploratory data analysis technique. *Geol. Explor.* **1993**, *11*, 52–58, (In Chinese with English Abstract).
70. He, W.; Luo, X.R.; Ouyang, F.; Liu, P.F.; Su, Y.H.; Hang, W.B. A study of geoelectrochemistry in search for concealed copper-nickel deposits in Hejiaya area, Lueyang County, Shaanxi Province. *Geophys. Geochem. Explor.* **2020**, *44*, 523–532. (In Chinese with English Abstract).
71. Kang, J.; Chen, L.M.; Song, X.Y.; Dai, Z.H.; Zheng, W.Q. Trace elements in olivines from the giant Jinchuan Ni-Cu (PGE) deposit, NW China, and its geological implication. *Adv. Earth Sci.* **2019**, *34*, 382–398, (In Chinese with English Abstract).
72. Ripley, E.M.; Sarkar, A.; Li, C.S. Mineralogic and stable isotope studies of hydrothermal alteration at the Jinchuan Ni-Cu deposit, China. *Econ. Geol.* **2005**, *100*, 1349–1361. [CrossRef]
73. Burgisser, A.; Degruyter, W. Chapter 11—Magma Ascent and Degassing at Shallow Levels. In *The Encyclopedia of Volcanoes*, 2nd ed.; Sigurdsson, H., Ed.; Academic Press: Amsterdam, The Netherlands, 2015; pp. 225–236.
74. Sparks, R.S.J. The dynamics of bubble formation and growth in magmas: A review and analysis. *J. Volcanol. Geot. Res.* **1978**, *3*, 1–37. [CrossRef]
75. Iacono-Marziano, G.; Le Vaillant, M.; Godel, B.M.; Barnes, S.J.; Arbaret, L. The critical role of magma degassing in sulphide melt mobility and metal enrichment. *Nat. Commun.* **2022**, *13*, 2359. [CrossRef]
76. Barnes, S.-J.; Lightfoot, P. Formation of magmatic nickel-sulfide ore deposits and processes affecting their copper and platinum-group eelement contents. *Econ. Geol.* **2005**, *100*, 179–213.
77. Taranovic, V.; Ripley, E.M.; Li, C.; Rossell, D. Chalcophile element (Ni, Cu, PGE and Au) variations in the Tamarack magmatic sulfide deposit in the Midcontinent Rift System: Implications for dynamic ore-forming processes. *Miner. Depos.* **2016**, *51*, 937–951. [CrossRef]